OXFORD

Imaging the columnar functional organization of human area MT+ to axis-of-motion stimuli using VASO at 7 Tesla

Alessandra Pizzuti[1,2,*], Laurentius (Renzo) Huber[1], Omer Faruk Gulban[1,2], Amaia Benitez-Andonegui[3], Judith Peters[1],
Rainer Goebel[1,2,*]

[1]Department of Cognitive Neuroscience, Faculty of Psychology and Neuroscience, Maastricht University, The Netherlands,
[2]Brain Innovation, Maastricht, The Netherlands,
[3]MEG Core Facility, National Institute of Mental Health, Bethesda, MD, United States
*Corresponding authors: Alessandra Pizzuti and Rainer Goebel, Department of Cognitive Neuroscience, Faculty of Psychology and Neuroscience, Maastricht
University, The Netherlands. Email: a.pizzuti@maastrichtuniversity.nl and r.goebel@maastrichtuniversity.nl

Cortical columns of direction-selective neurons in the motion sensitive area (MT) have been successfully established as a microscopic feature of the neocortex in animals. The same property has been investigated at mesoscale (<1 mm) in the homologous brain area (hMT+, V5) in living humans by using ultra-high field functional magnetic resonance imaging (fMRI). Despite the reproducibility of the selective response to axis-of-motion stimuli, clear quantitative evidence for the columnar organization of hMT+ is still lacking. Using cerebral blood volume (CBV)-sensitive fMRI at 7 Tesla with submillimeter resolution and high spatial specificity to microvasculature, we investigate the columnar functional organization of hMT+ in 5 participants perceiving axis-of-motion stimuli for both blood oxygenation level dependent (BOLD) and vascular space occupancy (VASO) contrast mechanisms provided by the used slice-selective slab-inversion (SS-SI)-VASO sequence. With the development of a new searchlight algorithm for column detection, we provide the first quantitative columnarity map that characterizes the entire 3D hMT+ volume. Using voxel-wise measures of sensitivity and specificity, we demonstrate the advantage of using CBV-sensitive fMRI to detect mesoscopic cortical features by revealing higher specificity of axis-of-motion cortical columns for VASO as compared to BOLD contrast. These voxel-wise metrics also provide further insights on how to mitigate the highly debated draining veins effect. We conclude that using CBV–VASO fMRI together with voxel-wise measurements of sensitivity, specificity and columnarity offers a promising avenue to quantify the mesoscopic organization of hMT+ with respect to axis-of-motion stimuli. Furthermore, our approach and methodological developments are generalizable and applicable to other human brain areas where similar mesoscopic research questions are addressed.

Key words: 7 Tesla; columns; fMRI; mesoscale; V5-hMT+.

Introduction

An important task of the visual system is to recognize moving objects in a dynamic environment. The macaque middle temporal (MT) area and its homolog in humans (hMT+, V5) is a higher order cortical visual area sensitive to the direction of motion (Zeki 1974, Maunsell and Van Essen 1983, Watson et al. 1993, Rees et al. 2000, Born and Bradley 2005, Zimmermann et al. 2011). It also plays an important role in constructive motion perception as revealed by illusory (e.g. apparent) motion stimuli (Goebel et al. 1998, Muckli et al. 2002, Born and Bradley 2005, Schneider et al. 2019). Invasive electrophysiological recordings (Albright et al. 1984, Diogo et al. 2003) and optical imaging (Malonek et al. 1994) results suggested that macaque extrastriate area MT is functionally organized in cortical columns, similarly to V1 (Hubel and Wiesel 1965). In particular, Albright et al. (1984) demonstrated in macaque MT the occurrence of a systematic relationship between the penetration angle of the electrode and the rate of change of preferred direction of motion, indicating that cells with a similar preference are arranged in vertically oriented columns (Mountcastle 1997, Buxhoeveden and Casanova 2002). Albright et al. also discovered that opposing directions of motion are located in neighboring columns forming larger axis-of-motion columns.

The advent of magnetic resonance imaging opened the avenue to bridge the gap to animal literature, by non-invasively investigating the functional organization of the human brain. Especially the advent of ultra high field (UHF) functional magnetic resonance imaging (fMRI) combined with recent advances in MR hardware and pulse sequences offers sub-millimeter spatial resolution (Uğurbil et al. 2003, Shmuel et al. 2007, Uludağ et al. 2009, Koopmans and Yacoub 2019) providing a unique way to unveil mesoscopic properties underlying cognitive functions at the level of cortical layers and cortical columns (Rakic 2008, Ugurbil 2016, Petro and Muckli 2017, De Martino et al. 2018, Dumoulin et al. 2018, Huber et al. 2020, Uğurbil 2021, Viessmann and Polimeni 2021, Cho et al. 2022). Mesoscopic 7T fMRI (Zimmermann et al. 2011, De Martino et al. 2013) has already been used to investigate the columnar organization of human MT using 3D-GRASE (Oshio and Feinberg 1992, Feinberg et al. 1995, Kemper et al. 2015) and blood oxygenation level dependent (BOLD) contrast. Zimmermann et al. (2011) provided the first direct demonstration of axis-of-motion selectivity and tuning characteristics in the human brain together with first insights into the spatial organization of hMT+. However, their columnar results can only be seen as an early approximation,

since their limited number of samples across cortical depth could obscure the full arrangement of the vertical columnar property. To validate and enhance previous findings, we investigate the functional organization of hMT+ in humans perceiving axis-of-motion stimuli using 3 improvements: (i) we use cerebral blood volume (CBV)-sensitive fMRI in addition to conventional BOLD fMRI, and we developed novel methods to (ii) quantify local sensitivity and specificity, and (iii) to detect, characterize, and visualize cortical columns.

CBV-sensitive fMRI. We use the SS-SI VASO (Huber et al. 2014) pulse sequence to get high-resolution CBV-sensitive fMRI. The VASO sequence is more suitable for imaging mesoscopic features compared to standard gradient echo BOLD echo planar imaging (GE-BOLD EPI), since it provides higher spatial specificity to the neuronal activation cite (Huber et al. 2019). Differently from the BOLD contrast, VASO is more sensitive to the microvasculature and it is less compromised by both oxygenation related vascular changes as well as large draining effects from vessels penetrating the cortex orthogonally or from pial veins lying on top of the gray matter surface (Duvernoy et al. 1981, Lauwers et al. 2008, Weber et al. 2011). However, its usage at submillimeter resolution is still challenging due to its inherently low signal-to-noise ratio (SNR) (Huber et al. 2019).

Local measure of sensitivity and specificity. For more precise quantification of differences between BOLD and VASO fMRI responses, we develop a voxel-wise measure of sensitivity and specificity as an extended version of the conventional global measures (Huber et al. 2017, Beckett et al. 2020). These metrics were also used to compare results from BOLD and VASO contrast mechanisms at the global level (Huber et al. 2017, 2020, Oliveira et al. 2022). Global metrics summarize the behavior of an entire region of interest, whereas our local metrics provide a functional characterization for each voxel inside a region of interest, resulting in more complete information for addressing mesoscopic questions at submillimeter resolution. More specifically, our new local metrics allow to evaluate the tuning property encoded in each voxel: if a voxel is strongly tuned to a specific condition its specificity will be high and its sensitivity will be inherited by the contrast mechanism, whereas if a voxel is poorly tuned, as in the case of a voxel sampling a big vessel, the specificity will be very low while the sensitivity will be very high.

Novel method to characterize cortical columns. To overcome depth-sampling limitations (Zimmermann et al. 2011), we develop a new searchlight algorithm for functional column detection that inspects the whole cortical depth of a specific volume of interest and provides a quantitative columnarity map that is useful to detect highly columnar functional patches inside the volume. The algorithm provides a new generalized framework for investigating the columnar functional organization for any cortical gray matter ribbon and it can potentially improve the replicability and comparability of columnar results across studies using a variety of columnar quantification methods (Yacoub et al. 2008, Zimmermann et al. 2011, De Martino et al. 2013, 2015, Schneider et al. 2019).

In this study, we acquire ultra-high field (7 Tesla) fMRI at submillimeter resolution (0.8 mm isotropic) to investigate the axis-of-motion cortical columns in hMT+ (V5). By using our new algorithm for column detection, we provide a quantitative columnarity map that fully characterizes the functional organization of hMT+ with respect to axis-of-motion preference. We demonstrate the advantage of using CBV-sensitive fMRI to detect mesoscopic cortical features by showing the higher specificity of axis-of-motion cortical columns detected by VASO compared to BOLD contrast.

Materials and methods
Experimental design

Participants. Five healthy participants (4 males and 1 female, 28–34 years old, 10 hMT+ regions) with normal or corrected-to-normal vision were recruited for the study. Participants received a monetary reward. All participants had been in an MRI scanner at least once before and were trained and experienced at maintaining fixation for long periods of time. Informed consent was obtained from each participant before conducting the experiment. The study was approved by the ethics review committee of the Faculty of Psychology and Neuroscience (ERCPN) of Maastricht University and experimental procedures followed the principles expressed in the Declaration of Helsinki. Note that the sample size of this study, despite it being small when compared to conventional fMRI studies, is well within the range used in previous fMRI studies at 7 T with similar research questions (Yacoub et al. 2008, De Martino et al. 2013, 2015, Schneider et al. 2019, Hollander et al. 2021, Haenelt et al. 2023).

Stimulus presentation. The scripts used for the stimulus presentation were developed based on Schneider et al. (2019) and presented using the open source application PsychoPy3 (v2020.2.4). Scripts are available on https://github.com/27-apizzuti/AOM-VASO_project. A frosted screen (distance from eye to screen: 99 cm; image width: 28 cm; image height: 17.5 cm) at the rear of the magnet was used to project the visual stimuli (using Panasonic projector 28 PT-EZ570; Newark, NJ, USA; resolution 1,920 x 1,200; nominal refresh rate: 60 Hz) that participants could watch through a tilted mirror attached to the head coil. We used 50% gray background (at 435 cd/m^2 luminance) with white dots (at 1310 cd/m^2) for the motion stimulation (black color is measured at 2.20 cd/m^2). An MR compatible button box was used to register participants' responses for the attention task during the entire functional scanning procedure.

Stimulus description. Each participant underwent a 2 h scanning session. In the scanning session, we collected 1 run to functionally locate hMT+, 3–4 runs (according to the available scanning time) to map 4 axes of motion conditions, and an MP2RAGE scan to obtain a high-resolution structural image (only if not already available from a previous scanning session). For the hMT+ functional localizer, a standard block design paradigm was used presenting moving dots in alternation with static dots in a circular aperture (Tootell et al. 1995) (run duration: 9 min 10 s). We did not separate MST from hMT (Huk et al. 2002, Kolster et al. 2010, Zimmermann et al. 2011) since we aimed to cover the whole human motion complex (hMT+). Dots traveled inwards and outwards from the center of the aperture for 10 s (speed = 8 degree of visual angle per second, dot size = 0.2 degree of visual angle, number of dots = 200, black dots on gray background), were followed by a stationary dots display presented for the same amount of time. A total of 27 repetitions of task-rest blocks were collected. For the axis-of-motion mapping runs, we presented dots in a circular aperture moving coherently along one of 4 axes (0° ↔ 180°, 45° ↔ 225°, 90° ↔ 270°, 135° ↔ 315°, in both directions of motion) (Zimmermann et al. 2011) alternated with static flickering dots (run duration: 15 min). Moving dot patterns (speed = 8 degrees of visual angle per second, dot size = 0.2 degree of visual angle, number of dots = 250) were presented for 24 s followed by a variable inter-trial interval (ITI) of 24–29 s to reduce functional signal carry over effects. Each motion axis block was repeated 4 times per run. In all conditions, a black disk (target/fixation dot) surrounded by an annulus was presented in the center of the aperture. Participants were instructed to fixate the black disk and respond through the button box every time
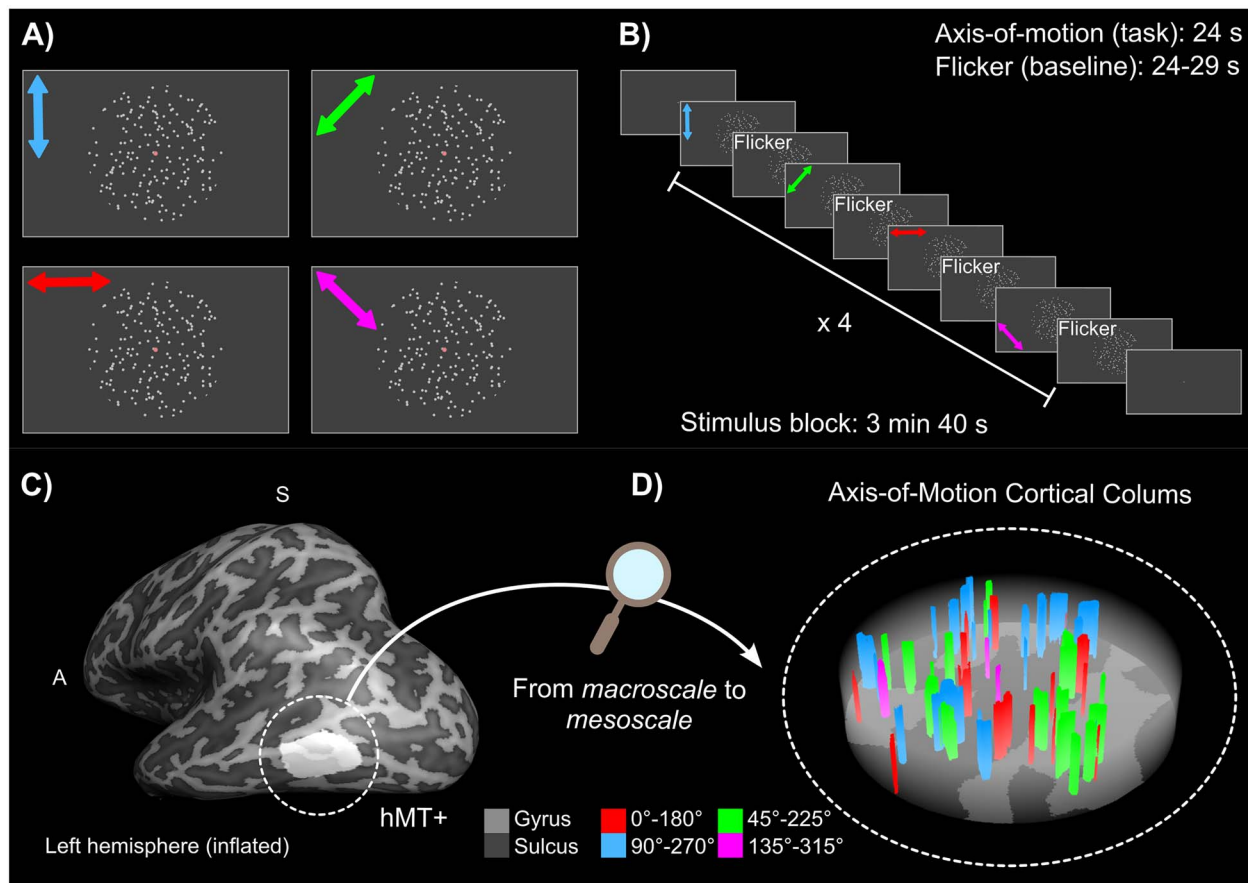
Fig. 1. Graphical abstract. A-B) Experimental paradigm. A) Moving dots stimuli were presented in a circular aperture moving coherently along one of four axes (colored arrows indicate 0°↔ 180°, 45°↔ 225°, 90°↔ 270°, 135°↔ 315°, in both directions of motion and were not presented in the actual stimulus). B) Within each stimulus block, all the four axis-of-motion conditions were presented in alternation with the flicker condition (baseline), for which dots were statically flickering. Each stimulus block was repeated four times in a run. A demo of our axis-of-motion stimulus is available here: https://github.com/27-apizzuti/AOM-VASO_project/tree/main/stimulus_scripts/demos. C-D) From macroscale to mesoscale. C) Definition of the region of interest hMT+, shown for an inflated hemisphere for one example participant (sub-01). D) Zooming in hMT+: example of axis-of-motion cortical columns shown for a flattened hMT+ for the same participant (sub-01).

the annulus changed color (attention task). Figure 1 provides an overview of the study as a graphical abstract. A demo of our axis-of-motion stimulus is available here: https://github.com/27-apizzuti/AOM-VASO_project/tree/main/stimulus_scripts/demos.

MRI acquisition

Data acquisition was performed on a whole-body "classical" MAGNETOM 7T (Siemens Healthineers, Erlangen, Germany) at Scannexus B.V. (Maastricht, The Netherlands) using a 32-channel RX head-coil (Nova Medical, Wilmington, MA, USA). A second and a third order B0 shimming procedure was used to improve the homogeneity of the main magnetic field B0 in the shim volume containing the region of interest. The localizer experiment was conducted using a GE EPI sequence with BOLD contrast (Moeller et al. 2010) (echo time (TE) = 15 ms, nominal flip angle (FA) = 55°, echo repetition time (TR) = 1000 ms, multi band factor (MB) = 3, 57 slices) with a whole brain field of view and a (98 × 98) matrix at 2 mm isotropic nominal resolution. Before the acquisition of the run, we collected 5 volumes for distortion correction with the settings specified above but opposite phase encoding (posterior-anterior).

For the axis-of-motion mapping experiment, we used a Vascular Space Occupancy (VASO) sequence (Lu et al. 2003) optimized

for 7T (Hua et al. 2011). Specifically, we used the Slice-Selective Slab Inversion (SS-SI VASO) approach (Huber et al. 2014) with a 3D EPI readout (Poser et al. 2010) at nominal isotropic voxel resolution of 0.8 mm. Previous work has shown that the 3D readout is beneficial for sub-millimeter applications (Huber et al. 2018). The in-plane field of view was 129×172 mm (162×216 matrix) for a total of 26 acquired slices. The imaging parameters were: TE = 25 ms, 'temporal resolution' of pairs of images = 4840 ms, variable flip angle scheme FA = 26+°, in plane partial Fourier factor 6/8 with POCS reconstruction of 8 iterations, inversion time (TI)=1530 ms for the blood nulling point and FLASH-GRAPPA = 3 (Talagala et al. 2016). Variable flip angles were used to minimize T_1-related blurring along the slice direction (Huber et al. 2018). The sequence was implemented using the vendor provided IDEA environment (VB17A-UHF) and is available to download via C2P on the SIEMENS App-Store in Teamplay. The placement of the small functional slab was guided by an online analysis of the hMT+ localizer data (general linear modeling by Siemens), to ensure a bilateral coverage of area hMT+ for every participant.

The anatomical images were acquired with an MP2RAGE (magnetization prepared 2 rapid gradient echoes) (Marques et al. 2010) at 0.7 mm isotropic resolution (TR/TE = 6000 ms/2.39 ms, TI = 800 ms/2750 ms, FA = 4°/5°, GRAPPA = 3). MP2RAGE sequence parameters are optimized to overcome the large spatial inhomogeneity

in the transmit B1 field by generating and combining in a novel fashion 2 different images at 2 different inversion times (TI1, TI2) to create T_1-weighted MP2RAGE uniform (UNI) images (Marques et al. 2010). Physiological traces of respiration and heartbeat were recorded but not used for the analysis, since we did not observe any improvements by conducting RETROICOR physiological noise correction during the piloting stage (Glover et al. 2000). Indeed, sub-millimeter data are expected to be in the thermal noise-dominated regime (Triantafyllou et al. 2005).

Structural data analysis
Preprocessing and registration
T_1-weighted UNI images with high contrast-to-noise ratio from MP2RAGE were used to guide the determination of the anatomical location of hMT+ and to derive layers in the cortical ribbon of interest. T_1-w UNI images were skull-stripped using a brain mask obtained by inputting the MP2RAGE INV2 (TI2) images to FSL BET (v.6.0.5) (Smith et al. 2004). When needed, we semi-automatically corrected the results and used Segmentator (v.1.6.0) (Gulban et al. 2018) to remove dura mater contribution. Then, we used the anatomical bias correction algorithm from SPM12 (Wellcome Trust Center for Neuroimaging, London, UK) to further reduce inhomogeneities in the T_1-w UNI images (Ashburner and Friston 2005, Friston et al. 2007). In order to preserve the high-resolution functional data from issues of registration and interpolation while computing depth-dependent analysis (Huber et al. 2017, Guidi et al. 2020), we aligned the T_1-w UNI images to the high-resolution functional VASO data, according to https://layerfmri.com/2019/02/11/high-quality-registration/. The target functional slab "T_1-w EPI" was derived from the original SS-SI VASO time series by computing the inverse of signal variability that provides a good contrast between gray matter (GM) and white matter (WM) using AFNI (v.20.3.01) (Cox 1996, Cox and Hyde 1997) (function: -cvar). In ITK-SNAP (v.3.8) (Yushkevich et al. 2006) we manually aligned the T_1-w UNI whole brain images to the T_1-w EPI slab and then ran ITK-SNAP's automatic co-registration tool. Then, we used the obtained transformation matrix as input for running ANTS's "Syn" registration algorithm (v.20.3.01) (Avants et al. 2009, 2011, Madge 2020). Finally, the T_1-w UNI images were resampled to the T_1-w EPI space using ANTS b-spline interpolation (antsApplyTransforms -BSpline).

Segmentation
Accurate and precise tissue segmentation is a crucial step to investigate cortical layers and columns. Since conventional segmentation packages yielded unsatisfactory results for our restricted field of view, a semi-automated segmentation approach with manual intervention was used here. We used -3dresample command from AFNI (v.20.3.01) to upsample (with cubic interpolation) the processed T_1-w UNI images with an upscaling factor of 4 (nominal resolution = 0.2 mm isotropic). This step allowed a smoothed calculation of cortical features (e.g. curvature or thickness). Then, we confined the segmentation process to a "scoop of interest" in both hemispheres: in ITK-SNAP we centered a spherical mask around the anatomically expected area hMT+. We ran FSL FAST to obtain a first definition of the cerebro-spinal fluid/gray matter (CSF/GM) and the gray matter/white matter (GM/WM) tissue borderlines. Tissue labels were carefully quality controlled and manually edited when necessary (by A.P.), and later revised independently by another expert (O.F.G.). In combination, we also used morphological operations (dilation and erosion) (Virtanen et al. 2020) to further improve the segmentation output. These operations, when applied in combination with the same parameters, remove mislabeled isolated voxels and smooth boundaries between tissues.

Cortical depths
Once the segmentation was completed, we used LN2_LAYERS program from LayNii (v2.2.1) (Huber et al. 2021) to compute equi-volume cortical depths (Bok 1959, Waehnert et al. 2014), cortical thickness and curvature for each gray matter voxel.

Flattening
We used LN2_LAYERS, LN2_MULTILATERATE, and LN2_PATCH_FLATTEN programs within LayNii to flatten our cortical patches (Gulban et al. 2022). We first establish the center of gravity of the gray matter activated ROIs (left and right hMT+). Then a disk of a predefined radius is grown geodesically and a local 2D coordinate system (U and V coordinates) was imposed on it (using LN2_MULTILATERATE program). Together with the "metric" file from LN2_LAYERS (D coordinate), the end result of this procedure is a full continuous mapping between flat cortex space (UVD) and the original folded cortex space (XYZ). This mapping allows us to flatten 3D chunks of cortical data (in NIfTI format) to explore mesoscopic cortical structures as it was done in previous studies (Zimmermann et al. 2011, De Martino et al. 2013, Schneider et al. 2019).

Functional data analysis: localizer experiment
Functional localizer data were pre-processed in BrainVoyager v.22.1 (Goebel et al. 2006, 2012) as follows: slice scan time correction, motion-correction, linear trend removal, and high-pass filtering (6 cycles). We corrected for EPI geometric distortion using the image registration method based on the opposite phase encoding direction EPI data as implemented in COPE BrainVoyager plugin (Breman et al. 2020). The same aligning procedure explained for structural images was also used to align functional localizer data to high-resolution VASO data. The registration parameters (ITK-SNAP, ANTS "Syn") were estimated matching the computed temporal mean image from localizer data (Smith et al. 2004) with T_1-w EPI and then applied to the time series using ANTS B-spline interpolation. Then, in order to functionally define our ROI (bilateral hMT+), we calculated a voxel-wise general linear model (GLM) for each participant in BrainVoyager. The GLM was corrected for temporal auto-correlation (AR2). The model contained a single predictor for the stimulus condition "moving dots" convolved with a standard hemodynamic response function. Voxels that showed a significant response to "moving vs static dots" contrast (using a threshold (q) corrected for multiple comparisons using false discovery rate; q(FDR) <.05) were selected. Finally, we defined a bilateral hMT+ ROI, by intersecting these voxels with two spheres of 16 mm in radius (one for each hemisphere) placed inside the expected anatomical location (Zimmermann et al. 2011, Schneider et al. 2019).

Functional data analysis: axes of motion experiment
Preprocessing and functional maps
Axis-of-motion functional data were analyzed following the optimized preprocessing pipeline for SS-SI VASO sequence https://layerfmri.com/2019/03/22/analysispipeline/. For each run, the first 4 time points (non-steady state images) were overwritten with steady-state images. Then, we separated odd and even time points from raw data, corresponding to MR signals with and without blood nulling and we separately performed motion

correction using SPM12 (Friston et al. 2007). A 4th-order spline was used for resampling to minimize blurring. For every participant, motion parameters between the two contrasts were very similar, as expected, and never higher than the nominal voxel resolution. The original time series length was restored for both blood-nulled and BOLD images using 7th order polynomial interpolation method before multiple runs were averaged to minimize noise amplification in the next processing steps. Dynamic division of blood-nulled and BOLD volumes was performed to generate VASO images with reduced BOLD contrast contamination (LN_BOCO program within LayNii). BOLD correction is valid under the assumption that T_2* contrast is the same in images with both contrasts, because they are acquired concomitantly (Huber et al. 2014). For each participant, we fit a voxel-wise general linear model restricted to the bilateral hMT+ ROI (previously defined) on both the BOLD and VASO time series in BrainVoyager. The model contained five predictors, one for each axis-of-motion condition and one for the flickering condition. Each predictor was then convolved with a standard hemodynamic response function. The GLM was corrected for temporal auto-correlation (AR2). Statistical t-maps were then computed. While generating the t-map by contrasting one axis-of-motion stimulus condition (e.g. horizontal) versus flickering dots baseline condition, the two contrasting conditions were balanced in terms of number of time points considered in the computation, since in the experimental paradigm the latter was repeated 4 times more than the former one. In addition to the t-maps, we also computed voxel-wise percent signal change (Huber et al. 2017, Beckett et al. 2020) between mean signal during task (e.g. moving dots along one axis-of-motion) and baseline (flickering dots) with the same balancing rationale used for computing t-maps. This method has been shown to provide results that are easier to interpret than methods using inferential statistics, which can be affected by laminar differences in noise and hemodynamic response function shape (Huber et al. 2017). We used percent signal change to computed layer profiles (results are presented in Supplementary Figs. 2 and 3).

Preference maps and voxel selection

We created a BOLD and VASO "preference map" (un-thresholded) by assigning to each voxel the preferred axis-of-motion, based on the predictor showing the highest GLM fit (among the four axes of motion), representing the highest stimulus-induced normalized fMRI response (t-value) (Zimmermann et al. 2011, De Martino et al. 2013, Schneider et al. 2019).

To take into account differences in sensitivity between the two contrast mechanisms, we evaluate the hMT+'s tuning to axes of motion stimuli following three statistical ways and compare the obtained results.

We thresholded the preference maps by considering three sets of voxels (see Table 1): (i) voxels that exhibited a significant t-value response (using a threshold (q) corrected for multiple comparisons using false discovery rate; q(FDR) < 0.05) when contrasting "all axes of motion moving dots vs flickering dots," later called 'FDR'. (ii) Voxels that survive a cross-validation test, later called 'CV'. (iii) Voxels that survive a cross-validation test and show positive t-value response to each axis-of-motion condition, later called 'CV+'. A cluster-size thresholding (threshold = 4) was applied separately to each set of voxels (using https://gist.github.com/ofgulban/27c4491592126dce37e97c578cbf307b).

The number of "FDR" voxels differs significantly between the two contrast mechanisms, due to expected differences in sensitivity. As an alternative approach to the FDR method, we designed a leave-one-run out cross-validation method (Zimmermann et al. 2011, Emmerling 2016) that might be less dependent on the lower sensitivity of VASO. The cross-validation was separately applied to both BOLD and VASO preference maps restricted to suprathreshold BOLD "FDR" voxels. Iteratively, we divided the available number of runs (learning set) into training set (average of all runs excluding the test run) and test set (left out run) and for each set we labeled voxels according to their preferred axis, by fitting a GLM as explained above. Within each fold of the cross-validation process, only voxels showing the same axis preference between training and test set were kept for the next step. Finally, we cross-validated our BOLD and VASO preference maps by removing all voxels whose labeled preferred axis did not match with the cross-validated predicted label.

Our third method tackles the question about the neural meaning of having a negative response to a specific condition that was not taken into account for FDR and CV voxels. A negative response to a specific axis-of-motion could, in principle, indicate a neural suppression, as shown here Albright (1984). However, positive and negative t-value fluctuation around zero can also occur as noise contribution when dealing with low contrast-to-noise-ratio (CNR) data as it is the case for high-resolution fMRI. In order to exclude the latter possibility, we introduced the "CV+" set of voxels. In this case, we narrowed down the set of CV-voxels by only keeping those voxels that showed a positive response (t-value) for all conditions, when separately contrasting each axis-of-motion with the 'flickering condition'.

Tuning curves

Finally, for each set of voxels, tuning curves are computed for each axis-of-motion, by averaging t-values responses of all voxels sharing the same preferred axis-of-motion and evaluating them in the preferred and not preferred conditions. As previously done by (De Martino et al. 2013), a global tuning selectivity index was also computed for each tuning curve, by calculating the ratio of the response for the preferred axis-of-motion divided by the average response towards all other axes of motion.

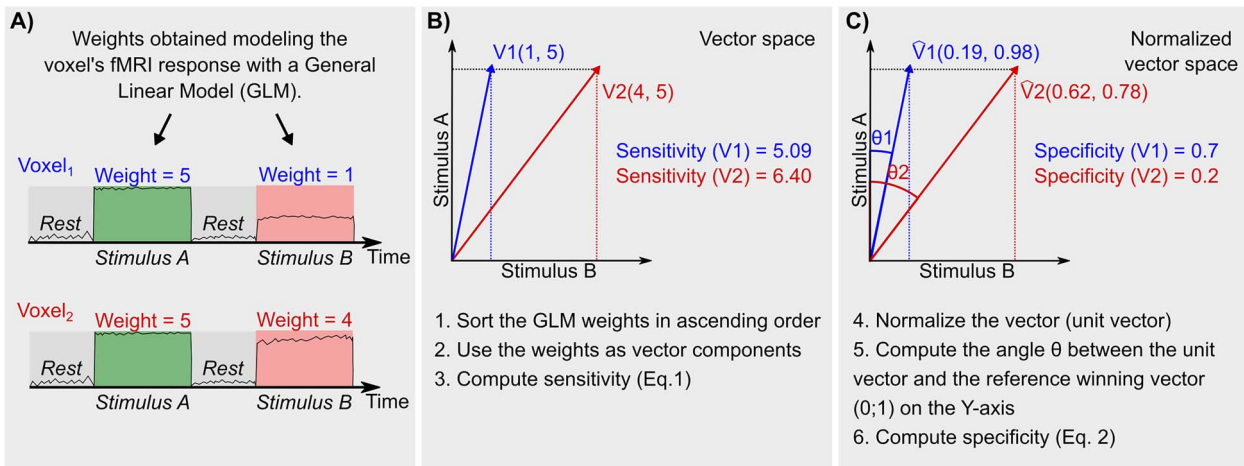### Voxel-wise sensitivity and specificity calculation

To investigate the signal behavior and differences between BOLD and VASO contrast, we developed new voxel-wise measures of sensitivity and specificity. By coding the voxel response to each axis-of-motion with a t-value, a 4 entries t-value vector was assigned to each voxel. Sensitivity was computed by calculating the Euclidean norm of the t-values vector ($\vec{v}$) (Eq. 1):

$$Sensitivity \overset{\text{def}}{=} \| \vec{v} \| \tag{1}$$

Specificity was computed according to Eq. 2:

$$Specificity \overset{\text{def}}{=} 1 - \frac{\arccos{(\hat{v} \cdot \hat{w})}}{\theta_{max}} \tag{2}$$

First, the t-values vector is transformed into a "unit vector" by dividing each component with the norm of the vector (from v to $\hat{v}$). Then, the entries of the vector were arranged in ascending order and the dot product between ($\hat{v}$) and a reference winning vector was computed [0 0 0 1] ($\hat{w}$). Since the ordering operation constrains

Fig. 2. Numerical example of how to compute voxel-wise sensitivity and specificity for a 2 dimensional case. In A) the fMRI response of a voxel is modeled using a General Linear Model and the response modulation or "weight" (e.g. beta, t-value, percent signal change) during each stimulus is computed. In B) and C) we show step-by-step how to use the weights to compute our voxel-wise sensitivity and specificity.

the angle computation in the range 0°-60° (in 4 dimensions), we scaled the computed angle by the maximum angle (θ_{max}). Finally, we defined "specificity" as the additive inverse of the computed scaled angle.

In Fig. 2, we show with two numerical examples how to compute step-by-step our voxel-wise sensitivity and specificity measures. Note that θ_{max} for the 2D case is equal to 45°. The sensitivity measure quantifies how strongly a voxel responds to any axis-of-motion condition. The specificity measure quantifies how well a voxel is tuned toward a specific axis-of-motion. We developed our specificity index (inspired by the n-dimensional compositional vector angle analysis from Gulban (2018)) which serves a similar purpose to the orientation selectivity index (OSI) commonly used in orientation tuning studies (Swindale 1998, Yacoub et al. 2008, Cho et al. 2022). The OSI is used when orientation tuning is investigated with a high orientation sampling (e.g. minimally every 45 degrees) in order to detect smooth changes in orientations, to fit a circular distribution and evaluate its dispersion from the preferred orientation. However, the OSI is not suitable for axis-of-motion paradigms since they do not differentiate functional responses to opposite motion orientation and, as consequence, do not provide a continuous sampling of the tuning response. In contrast, our specificity measure does not require a fitting and therefore may be considered as an alternative way to quantify voxel selectivity even in cases when categorical (and not continuous) stimulations are evaluated. For the specificity index calculation, negative t-value entries are a critical point. We assume that negative t-values represent, in our data, an absence of neural response to a specific condition, therefore, when occurring in FDR and CV set of voxels, we zero them. The CV+ set of voxels does not suffer from this limitation and functions as control.

The inset at the upper right corner of Fig. 5A visualizes the relationships between these 2 variables: voxel characteristics strongly differ according to which region of the space they belong to. For instance, high-tuned voxels are represented with high specificity, whereas un-specific vessel-dominated voxels are represented by high sensitivity and low specificity.

To test if it is possible to derive information about the vasculature from our fMRI data, we combined sensitivity and specificity information with time-averaged T_2^*-weighted EPI intensity from BOLD time series, since it was demonstrated to be a robust marker

of vascular effects (Kay et al. 2019). Global measures of sensitivity and specificity were also implemented to compare our results to the literature (Huber et al. 2017, Beckett et al. 2020).

Voxel-wise columnarity index calculation

Cortical column detection and quantification using fMRI is a challenging task (Yacoub et al. 2008, Zimmermann et al. 2011, De Martino et al. 2015, Schneider et al. 2019). Inspired by Blazejewska et al. (2019), we implemented a searchlight algorithm to seek cylindrical columnar structures following the local coordinates of the cortical gray matter. The introduction of a geodesically parametrized cylindrical kernel centered around each voxel in the folded brain instead of using rectangular kernels in the flattened domain (e.g. De Martino et al. (2015)) streamlines the columnarity index computation while at the same time making it easier to physically interpret. This algorithm is implemented as a part of LN2_UVD_FILTER program (accessible via "-columns" option) in LayNii v2.2.1 and consists of the following steps:

1) Our primary inputs are the local coordinates of the cortical gray matter. These local coordinates consists of: (i) a voxel-wise parametrization of the cortical surface that contains the orthogonal U and V coordinates (computed by LN2_MULTILATERATE program), and (ii) voxel-wise equi-volume cortical depths that contains the D coordinates ("metric" file output as computed by LN2_LAYERS program) (see Fig. 3A).

2) Our secondary input is a scalar map. This scalar map consists of the BOLD or VASO preference map (see Fig. 3B).

3) Our tertiary input is a binary map which we refer to as "domain". This binary map consists of the initial set of tuned voxels (the "FDR BOLD" voxels were used as mask for both BOLD and VASO contrast, see definition in the method section "Preference maps and voxel selection"). Note that we extended these activated voxels to cover the rest of the cortical thickness (using LN2_UVD_FILTER with "-max" option). For instance, if only a single middle gray matter voxel is available at a location, we include the voxels above and below until it covers the local cortical thickness.

4) The algorithm starts by evaluating a cylindrical 3D window centered at every voxel within the domain. This evaluation
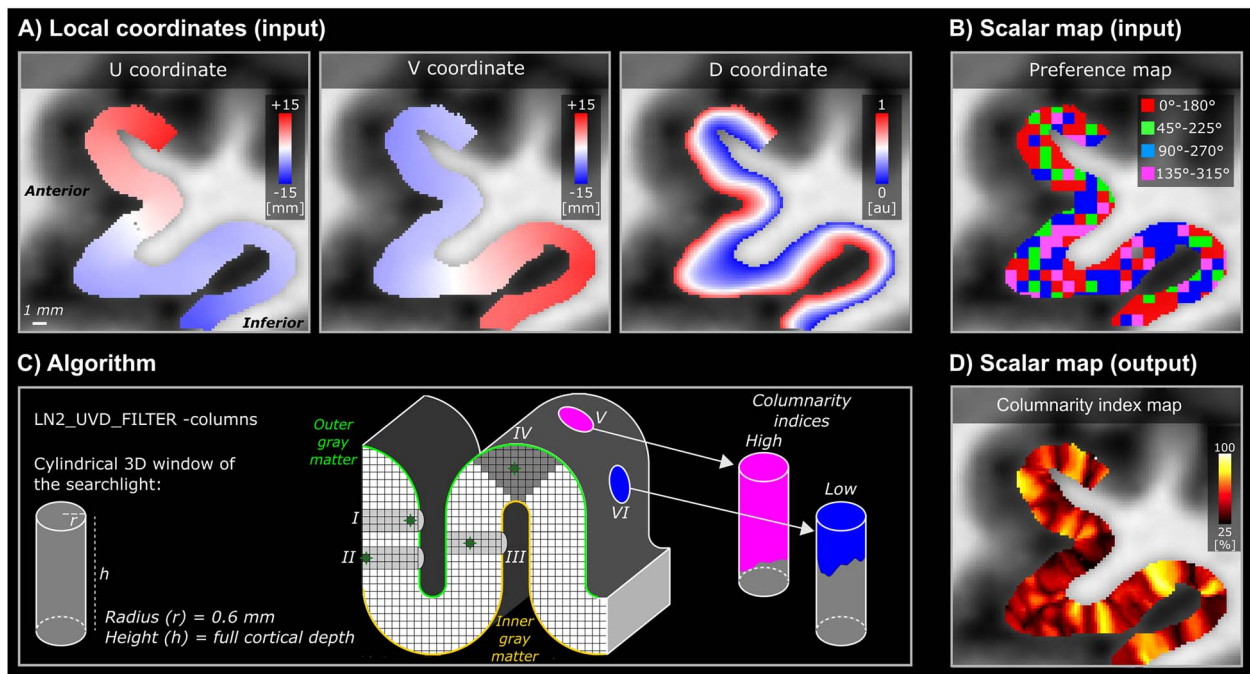
Fig. 3. Overview of the searchlight algorithm for functional cortical column detection. A-B) Input examples of local coordinates (U, V, D) and BOLD preference map of left-hMT+ for one example participant (sub-01). C) Conceptualization of the algorithm on a toy model of a cortical ribbon. A searchlight with a cylindrical 3D window is evaluated at each voxel position. On the toy model, we show the searchlight (dark gray voxels with cardinal axes) and its relative 3D window (light gray). For every position of the searchlight, the window adapts to the geometry of the ribbon and covers the entire cortical depth (see examples (I) voxel close to the outer gray matter, (II) voxel close to the inner gray matter, (III) voxel close to the middle gray matter on a wall, (IV) voxel close to the middle gray matter on a gyrus). Pink cylinder is an example of a high columnarity index (V), whereas the blue cylinder is an example of a low columnarity index (VI). D) Output example of the columnarity index map generated for the data (B) of the same participant.

is done by (i) computing Euclidean distances using the UVD coordinates of the center voxel to all the other voxels within the domain, and (ii) by detecting the voxels that fall within user-determined radius and height of the cylinder. Note that we set the cylinder radius to 0.6 mm and the height to cover the full cortical depth (independent of a voxel being at the deep, middle, or superficial part of the cortex, see number I, II, III, IV in Fig. 3C). We chose the diameter of the cylinder to be slightly higher than the nominal resolution (0.8 mm) in order to take into account all the possible orientations that a voxel can assume to sample the brain geometry (our diameter 1.2 mm is in the range: $\sqrt[2]{2} \times 0.8$ mm = 1.13 mm and $\sqrt{3} \times 0.8$ mm = 1.38 mm).

5) This step determines a set of voxels for each window. Note that the number of windows is equal to the number of voxels within the domain input. However, the total number of voxels for each window can change as a function of local cortical thickness and local curvature. Note that this behavior is natural and expected.

6) For the set of voxels within each window, we compute the modal (most frequently occurring) value within the BOLD or VASO preference maps.

7) Finally, we compute the "columnarity index" by dividing the number of voxels of the modal value with the total number of voxels evaluated in the cylindrical window (see Fig. 3D). Note that the columnarity index ranges between 0 (no columnarity) to 1 (ideal or pure columnarity).

Upon completion, our algorithm yields a map where each voxel contains a unique columnarity index. This procedure allows us to reveal cortical columns for any range of the columnarity index (from 0 to 1, with 0.5 step size) by accordingly thresholding the

columnarity map and applying it as a binary mask to the input preference map.

We summarize the columnar behavior of hMT+ for both BOLD and VASO contrast by providing the following quantitative measurements as a function of the columnarity index: voxel-wise sensitivity and specificity (see Fig. 9A and B (i–ii)) and percentage of columnar volume with respect to the volume of the domain (see Fig. 9A and B (iii)). Finally, we evaluate the spatial similarity between BOLD and VASO columnarity maps by computing a spatial consistency score: for each value of the columnarity index we quantify the percentage of voxels that appear in the same spatial location and with the same axis-of-motion preference in both contrasts with respect to the total amount of columnar voxels (see Fig. 9A, B (iv)).

Control analysis: benchmarking columnarity index calculation

In order to interpret the columnar results from the empirical BOLD and VASO functional data in terms of vicinity to a "pure noise" or to an "ideal columnar" scenario, we ran our columnarity index computation on two synthetic scalar maps ("noise" preference map and "ideal" preference map) and compared empirical vs benchmark results. This procedure was done for each empirical hMT+ separately (i.e. 10 hMT+ regions from the left and right hemisphere of five participants). The "random" preference map was generated at original voxel resolution (0.8 iso mm) by assigning to each voxel a preferred axis-of-motion based on a random distribution and then upsampled, as done for the empirical data. The "ideal" preference map that would lead to "ideal" functional columns was created by using the LN2_HEXBIN program from LayNii. This program uses the U,V coordinates of a specific

Table 1. Number of BOLD and VASO voxels considered for each voxel selection method (FDR, CV, CV+).

Left-hMT+	BOLD			VASO		
	FDR	CV	CV+	FDR	CV	CV+
sub-01	1168	444	404	88	302	157
sub-02	1245	388	370	66	203	82
sub-03	1006	394	383	48	258	88
sub-04	549	191	184	9	141	55
sub-05	756	286	261	149	256	123
Right-hMT+	BOLD			VASO		
	FDR	CV	CV+	FDR	CV	CV+
sub-01	976	384	361	25	157	54
sub-02	1159	410	391	9	226	75
sub-03	1082	439	430	40	262	107
sub-04	419	133	127	4	74	25
sub-05	1152	497	476	28	234	85

Table 2. Tuning Selectivity Index reported for both BOLD and VASO and each voxel selection method (FDR, CV, CV+).

Left-hMT+	BOLD			VASO		
	FDR	CV	CV+	FDR	CV	CV+
Horizontal 0°-180°	1.66	1.76	1.71	1.63	4.55	2.32
Vertical 90°-270°	1.66	1.81	1.75	1.8	3.71	2.31
Diagonal 45°-225°	1.62	1.67	1.65	1.75	4	2.16
Diagonal 135°-315°	1.58	1.67	1.62	1.74	3.86	2.23
Right-hMT+	BOLD			VASO		
	FDR	CV	CV+	FDR	CV	CV+
Horizontal 0°-180°	1.68	1.8	1.76	1.77	6.24	2.5
Vertical 90°-270°	1.62	1.71	1.68	1.69	5.87	2.37
Diagonal 45°-225°	1.57	1.64	1.62	1.9	6.15	2.5
Diagonal 135°-315°	1.56	1.65	1.63	1.75	4.43	2.37

brain volume to generate hexagonal bins with a desired radius spanning for the whole cortical depth. The hexagonal bins are considered as an approximation of "ideal" geometrically defined cortical columns. We chose 1 mm diameter to simulate columns that follow our hypothesis of axis-of-motion columns that can be unveiled by our current resolution. We compared columnarity index distributions from our empirical and benchmark data (results are presented in Fig. 10 and in Supplementary Fig. 4). Note that the generation of the benchmark dataset for both 'pure noise' and 'ideal columnar' scenario does not model the spatial covariance structure (point spread function) of our BOLD and VASO data but aims to benchmark our columnar method from its algorithmic point of view by providing fMRI contrast independent lower and upper bounds. Including the spatial covariance structure into the simulated noise might increase the lower bound, however such analysis is outside of the scope of the current work.

Results
Axis-of-motion tuning curves confirm direction-selectivity of hMT+

Participants performed well (97% accuracy) on the change detection task, indicating proper fixation throughout the experimental runs. The tuning property of hMT+ with respect to axis-of-motion stimuli was evaluated separately for both BOLD and VASO in three sets of voxels (FDR, CV, CV+). In Table 1, we report for each participant and hemisphere the number of voxels belonging to each set. We found bilateral axis-of-motion specific tuning curves for all three sets of voxels (FDR, CV, CV+) for both the BOLD and VASO contrast. As can be seen in Fig. 4, a characteristic peak at the preferred axis-of-motion is present in each group of voxels, showing a clear preference for a single axis-of-motion. Here we show, for the first time, that VASO is also sufficiently sensitive to map differential axes of motion responses in hMT+. Moreover, our BOLD results corroborate and extend previous fMRI BOLD findings (Zimmermann et al. 2011, De Martino et al. 2013, Schneider et al. 2019) showing robust responses of hMT+ to directions of motion.

For the BOLD contrast, varying the voxel selection method results in a subtle progressive increase in tuning selectivity index from the FDR to the CV and CV+ voxels (see Table 2). Figure 4 shows that the t-values of the preferred condition increases, while t-values for the non-preferred conditions decrease. We don't observe substantial differences when comparing the CV with CV+ BOLD voxels, since the voxel's reduction rate was always less than 10%. Our BOLD results consistently show the tuning selectivity of hMT+ being invariant to the voxel selection procedure.

For the VASO contrast, varying the voxel selection method from FDR to CV+ does not result in a progressive increase in tuning selectivity index. The tuning curves from the FDR voxels are characterized by the highest t-value range in both preferred and not preferred conditions. As a consequence, the tuning selectivity index is the smallest among the three sets and comparable with the ones computed for the BOLD contrast. The statistical threshold q(FDR) < 0.05 might be too conservative for the low sensitivity of the VASO contrast and only captures a subset of tuned voxels that are similarly activated in both contrasts. The tuning curves from the CV voxels are characterized by the highest tuning selectivity index. The percentage of surviving CV voxels around 24.8% (left-hMT+) and 19.2% (right-hMT+) was comparable with 35.8% (left-hMT+) and 37.6% (right-hMT+) for the BOLD contrast, suggesting that the partial recovery of the low sensitivity for the VASO contrast comes together with an increased tuning selectivity (see Table 2). However, when considering the VASO tuning curves using CV+ voxels, the tuning selectivity index is still higher than VASO FDR voxels, but it is lower when compared to VASO CV voxels. This effect might be due to the presence of negative t-values in the CV voxels, which might pull towards zero the t-values of the non-dominant conditions, inflating the tuning selectivity index. Although we found differences in tuning selectivity depending on the voxel selection, our results show tuning selectivity for both BOLD and VASO tuning curves with a slightly stronger selectivity effect for the VASO contrast.

Voxel-wise sensitivity and specificity metrics quantify differences in imaging contrast

We computed voxel-wise sensitivity and specificity for all FDR, CV, CV+ tuned voxels for both BOLD and VASO contrast in both hemispheres. As observed in Fig. 5 characteristic sensitivity–specificity scatter plots were found for both BOLD and VASO contrast. For all participants, we observed that BOLD cross-validated voxels are overall more sensitive (spanning a wider sensitivity range) and less specific (spanning a narrower specificity range) compared to VASO voxels. In line with our tuning curve results, the choice of the voxel selection does not affect the shape of both BOLD and VASO scatterplots. However, the strongest BOLD and VASO difference in sensitivity and specificity ranges are mostly observed
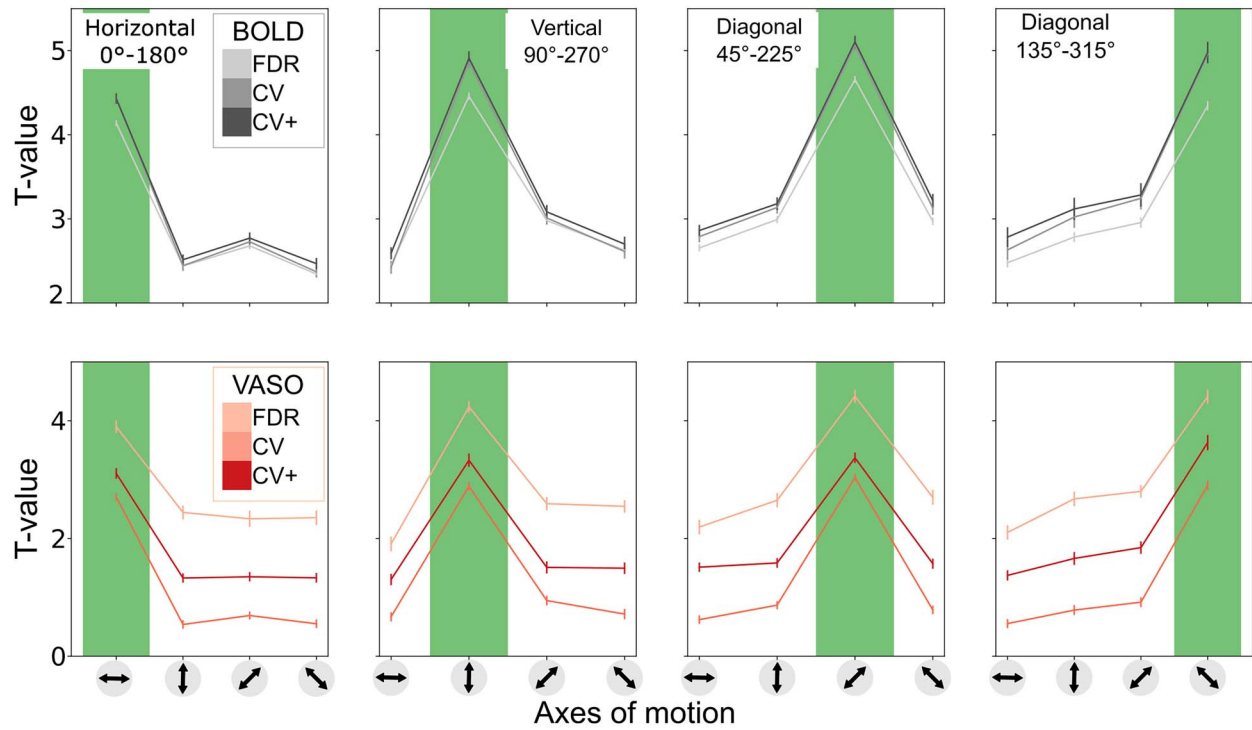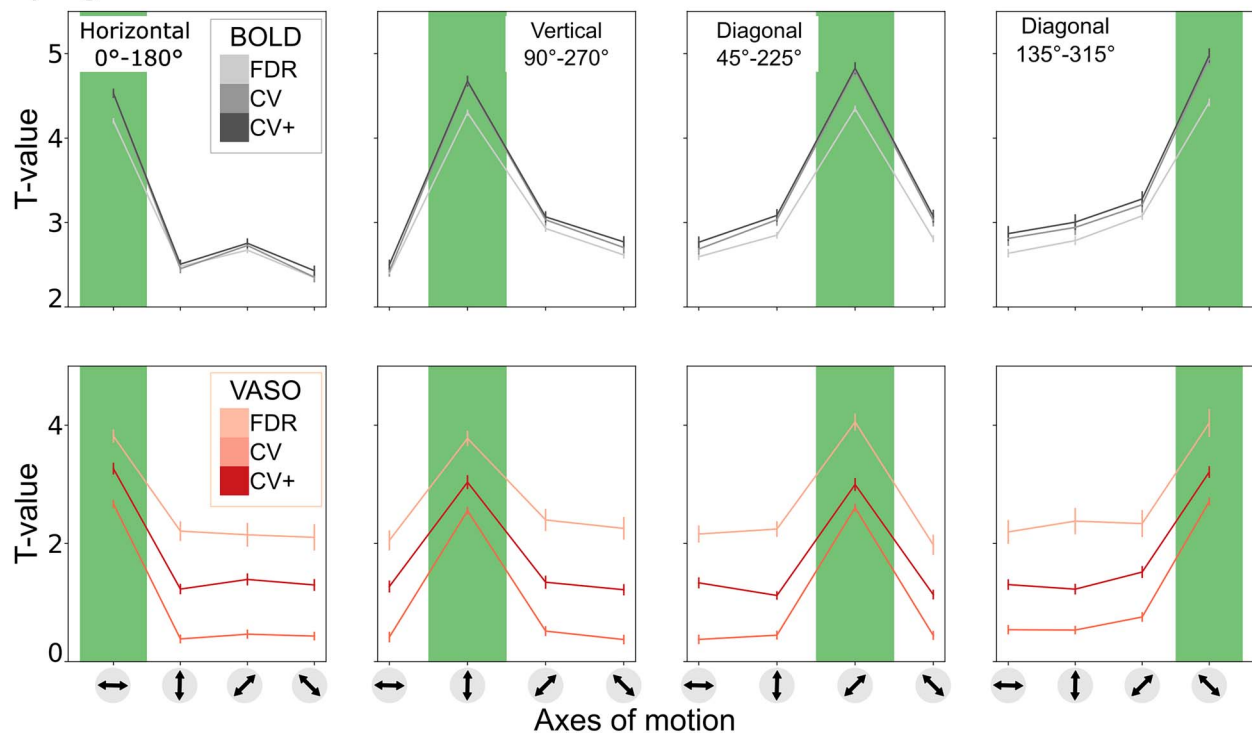
Fig. 4. Group average axis-of-motion selectivity tuning curves for each axis-of-motion for both BOLD and VASO contrast in the (A) left hMT+ and (B) right hMT+. Tuning curves are evaluated for FDR, CV and CV+ voxels. The plots depict the mean and the standard error of all voxels for each category.

for CV and CV+ voxels. Again, the FDR VASO voxels seem to be a subset of BOLD voxels.

Our results are in agreement with recent findings (Huber et al. 2017, Beckett et al. 2020) (see also Supplementary Figs. 2 and 3) and confirm that, despite its reduced signal sensitivity, the VASO contrast provides greater specificity to the neuronal origin

of the fMRI signal. Interestingly, our new local sensitivity and specificity measures offer a voxel-wise perspective on the draining veins effect: the vessel-dominated voxels responsible for this effect can be straightforwardly detected and localized. As shown for an exemplary participant in Fig. 6, the combination of high sensitivity and low specificity help detecting vessel-dominated
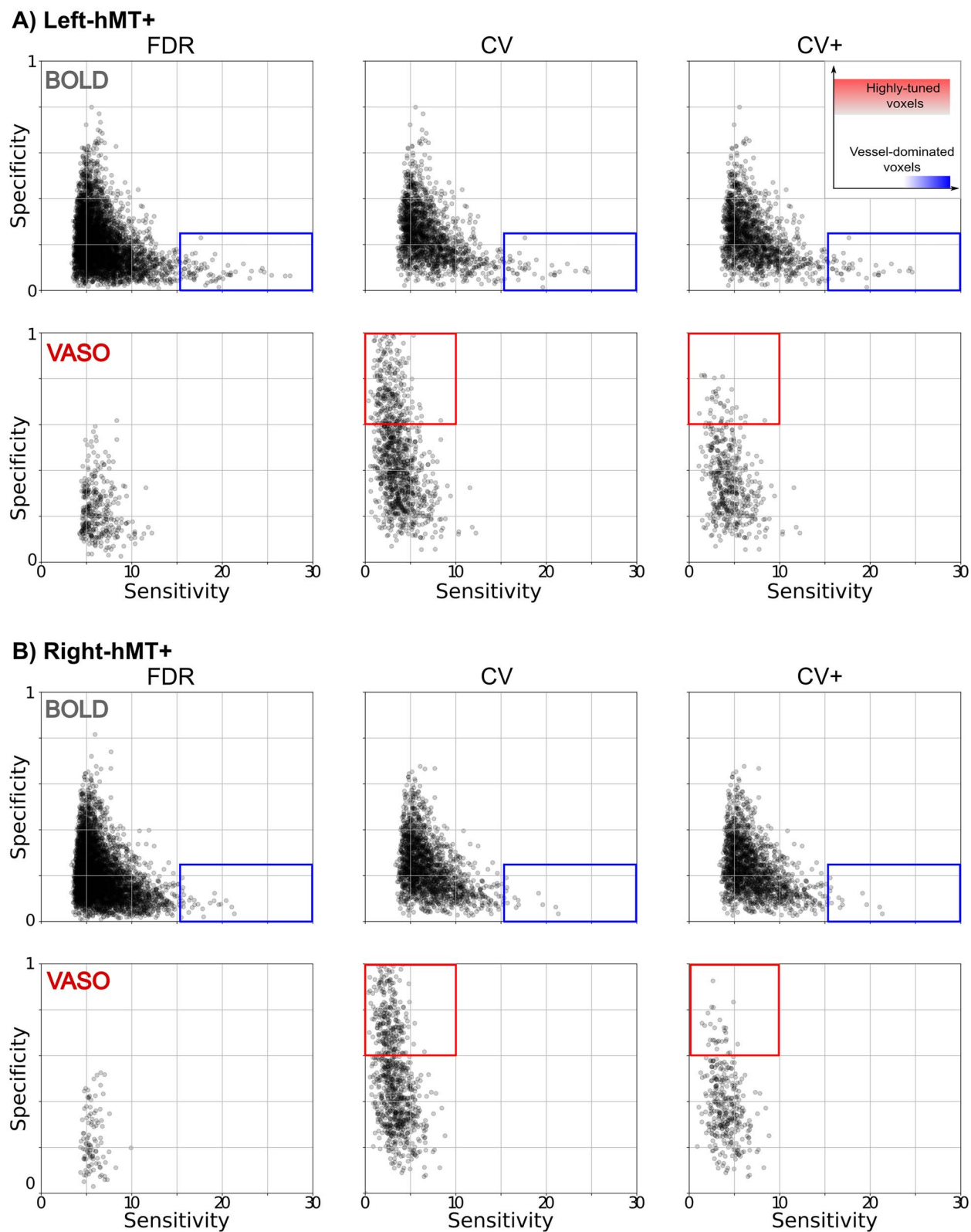
Fig. 5. Group result for sensitivity and specificity scatterplot for both BOLD and VASO contrast in (A) left hMT+ and (B) right hMT+ for FDR (right column), CV (middle column) and CV+ (right column) voxel sets. The inset at the upper right corner shows in a qualitative way how different regions of the space are associated with different voxel characteristics. Rectangles highlight main differences between contrast types and voxel selection strategy. The red rectangle encompasses highly tuned voxels, whereas the blue area shows vessel-dominated voxels.
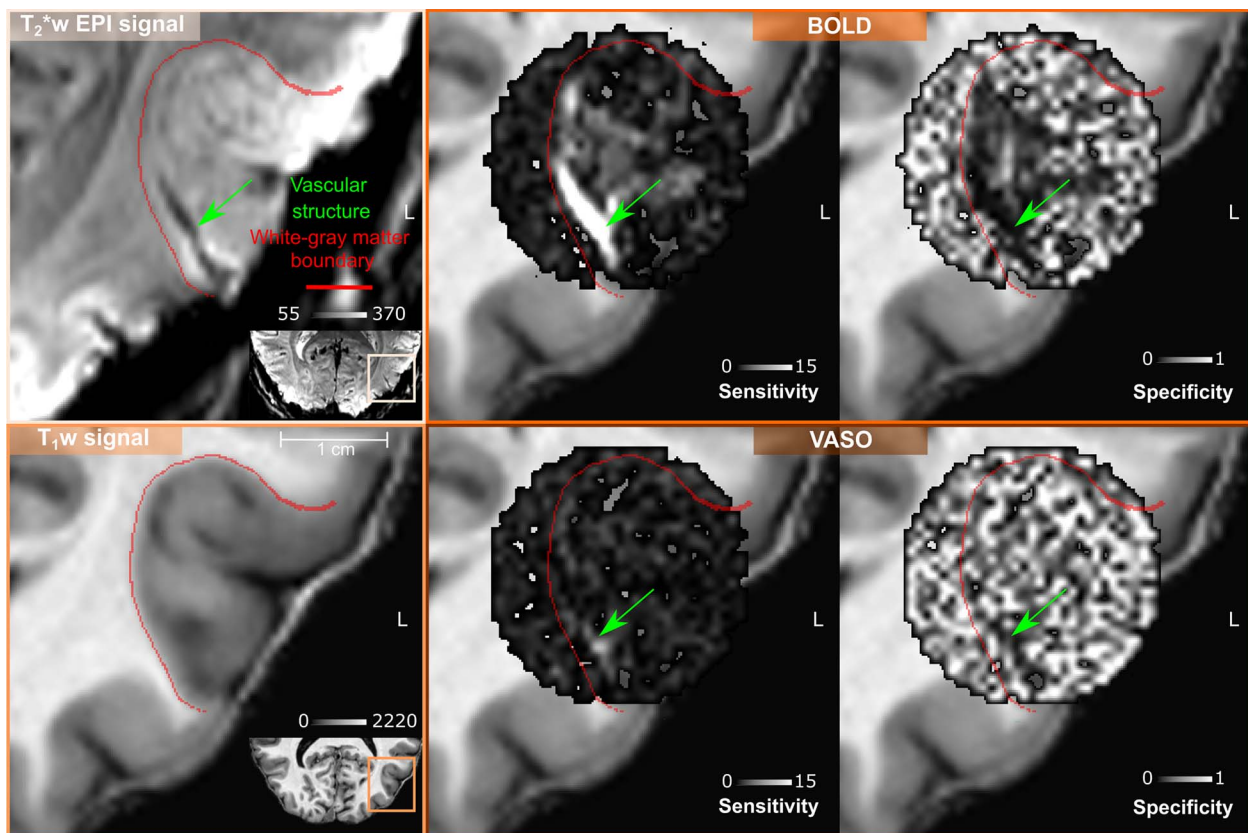
Fig. 6. Volume-based visualization of voxel-wise sensitivity and specificity maps for one example participant (sub-01) in the left hMT+ ROI. The same axial slice is shown for both T_2^*-w EPI signal and T_1-w signal (nominal resolution 0.2 iso mm). The green arrow points to a vascular structure detectable only through T_2^*-w EPI intensity as a dark spot (reflecting static susceptibility effects). High sensitivity and low specificity characterizes all the voxels belonging to this vascular structure (green arrows) for BOLD contrast. The detectability of this vascular structure is less evident for VASO contrast, as expected.

voxels (highlighted by green arrows) similarly to decreased BOLD T_2^*-weighted EPI intensity that has been shown to be a robust marker of vascular effects (Kay et al. 2019). A lower number of vessel-dominated voxels are found for VASO contrast compared to BOLD, demonstrating the reduced signal contamination by draining veins and its improved specificity. In Fig. 7, we project the vessel-dominated voxels shown in Fig. 6 in the flat laminar-resolved domain. This representation provides a more convenient visual representation to evaluate voxel localization across cortical depths. As shown in Fig. 7, the vessel-dominated voxels appear mostly in the superficial layers and disappear in the deep layers. This result demonstrates BOLD signal contamination by pial vasculature that lies above the cortex. The same phenomenon is strongly attenuated in VASO signal.

Quantification of the columnar organization of axes of motion tuned voxels

We explored the spatial organization of axis-of-motion tuned voxels for both BOLD and VASO contrast by using our new searchlight algorithm for column detection. We evaluated both BOLD and VASO columnarity maps as a function of the columnarity index. We used the flattening algorithm (Gulban et al. 2022) and 3D rendering visualization tools (Sullivan and Kaszynski 2019) to show our columnar results. The spatial organization of the columns can be fully observed in the rotated animations accompanying the Fig. 8: https://doi.org/10.6084/m9.figshare.20393667.

In Fig. 8A and B, we show BOLD and VASO axis-of-motion columnar results for one representative participant (left-hMT+)

for three values of the columnarity map 25%, 50%, 65%. Qualitatively, we observe that hMT+ is mostly organized by "small" columns or "patch of columns" occupying a quarter or a half of the whole cortical depth. For these columnarity index thresholds, we find that only a part of the columnar organization is preserved in both BOLD and VASO contrast (Fig. 8C). The density of the axis-of-motion columns decreases with a linear increase of the columnarity index for both BOLD and VASO.

To derive a quantitative description of the columnar organization of hMT+ with respect to the axis-of-motion stimuli, we summarized the group results of hMT+ in Fig. 9. According to our local measures of sensitivity and specificity, we confirm that VASO columnarity results are always more specific and less sensitive than BOLD columnarity results regardless of the choice of the columnarity index (Fig. 9A and B (i–ii)). Interestingly, we found that for a columnarity index of 40% the percentage of columnar volume reaches a peak for both BOLD and VASO contrast (Fig. 9A and B (iii)). At the same time, more than 50% of the columnarity maps are consistently found in both BOLD and VASO columnar results (Fig. 9A and B (iv)). Our results suggest that the selectivity of hMT+ is mostly organized in 'patches of columns,' and only partially organized in geometrically-defined columns spanning the whole cortical depth.

Finally, we compare our empirical results with the columnar results derived from the "random" and "ideal columnar" benchmark results and summarize them in Fig. 10. In Supplementary Fig. 4 we compare columnarity index's probability density
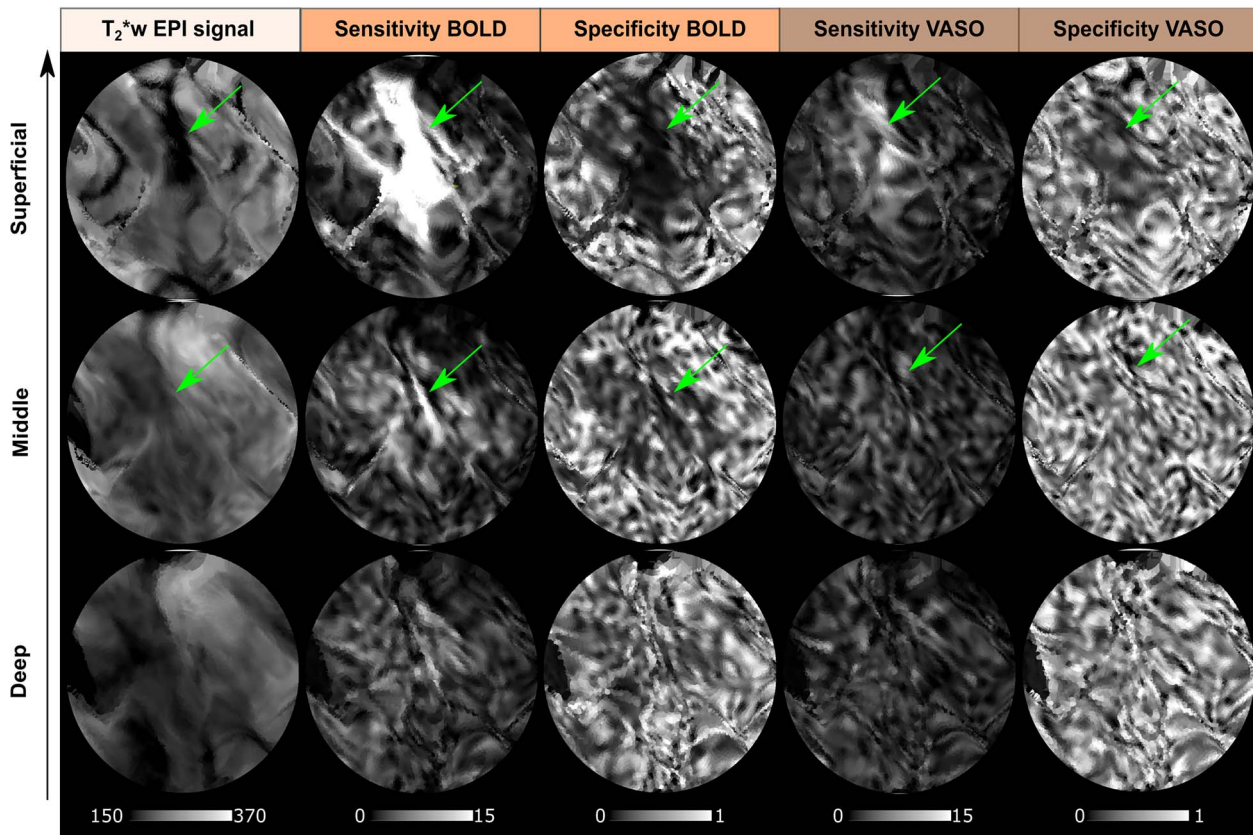
Fig. 7. Depth-dependent T_2*-w EPI intensity, voxel-wise sensitivity and specificity maps for BOLD and VASO contrast showed for the flattened left hMT+ ROI for one example participant (sub-01) (nominal resolution 0.05 mm iso.). Note that in this figure we project the same vessel-dominated voxels shown in Fig. 6 in the flat laminar-resolved domain. The vascular structure highlighted by the green arrow corresponding to the dark spot in T_2*-w EPI intensity is clearly visible at superficial layers but not at middle or deep layers, which indicates that it is a pial vein. High sensitivity and low specificity are in agreement with the spatial displacement of darkness of T_2*-w EPI intensity.

function (PDF) of empirical and benchmark data for each participant. As we can see for the group results in Fig. 10, the median of the distribution of the columnarity index for both BOLD and VASO is always in between the median of the distribution of the columnarity index of the "random" and the "ideal" benchmark datasets.

Discussion
Overview of the results

This study shows for the first time the feasibility of mapping axes of motion cortical columns in the extrastriate area hMT+ in living humans using CBV-VASO fMRI at 7T. The SS-SI VASO sequence with 3D EPI readout enabled us to simultaneously acquire BOLD and VASO responses in hMT+. Therefore, we separately applied the same analysis pipeline to both VASO and BOLD fMRI data (Huber et al. 2015, 2017, Oliveira et al. 2022). In this regard, the development of new local metrics of sensitivity and specificity was pivotal to quantitatively compare and interpret results found with VASO and BOLD contrast. Our metrics not only confirmed the higher specificity and lower sensitivity of VASO compared to BOLD voxels (Beckett et al. 2020), but also allowed us to clearly highlight pial vein effects in BOLD contrast. Finally, the new searchlight algorithm for functional column detection provides a unique framework to investigate mesoscopic cortical features with its improved quantifiability and comparability with

respect to previously used methodologies (Yacoub et al. 2008, Zimmermann et al. 2011, De Martino et al. 2013, 2015, Schneider et al. 2019). The columnarity map computed by our algorithm provides a full representation of the 3D functional organization of hMT+ allowing a transparent evaluation of columnarity.

Local vs global sensitivity and specificity metrics

Conventionally, global measures of sensitivity and specificity (Huber et al. 2017, Beckett et al. 2020) are used to compare different contrast mechanisms in terms of draining veins effects. As described in (Beckett et al. 2020) those global indices are computed by fitting a linear regression model to layer profiles (see Supplementary Fig. 3). In this work, we extended the concept of sensitivity and specificity from a global to a voxel-wise scale, by exploiting the tuning property of hMT+ voxels. By visualizing our sensitivity and specificity maps, we observed that untuned voxels show very low specificity. Voxels close to pial vessels show a very low specificity and very high sensitivity in combination with a low T_2*-w EPI signal as an additional independent diagnostic marker. For the data of the participant reported in Figs. 6 and 7, we clearly showed BOLD voxels sampling a pial vessel. The VASO contrast is expected to be not sensitive to macrovasculature. However, we still observe a smaller number of voxels with the aforementioned properties. Two possible candidate mechanisms can be leading to this phenomenon: a flow-dependent vein effect as described in (Huber 2015) or a dilatation effect of big arteries
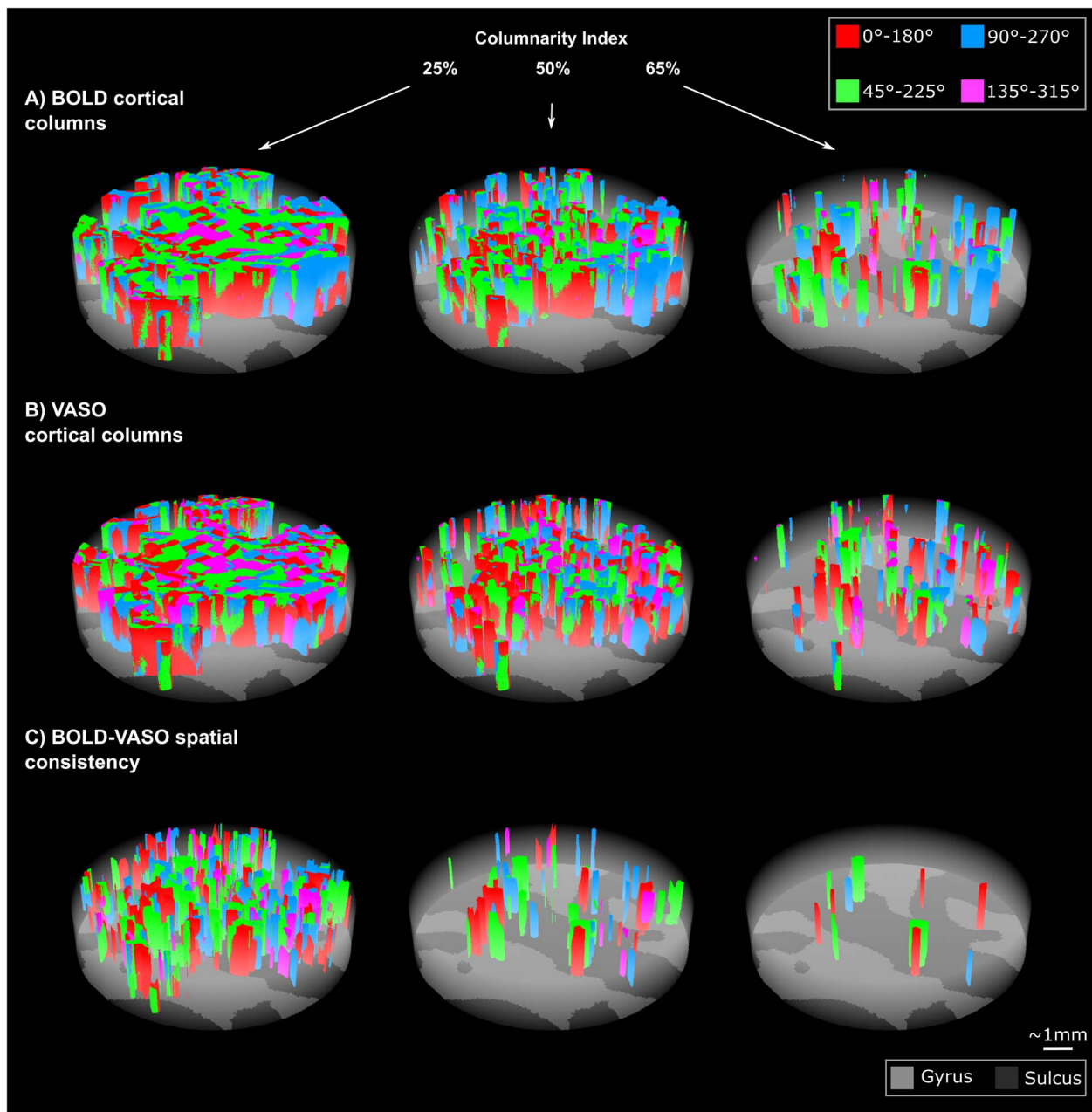
Fig. 8. Examples of BOLD (A) and VASO (B) axes-of-motion cortical columns for one example participant (sub-01) at 25%, 50%, 65% of the columnarity index. C) BOLD-VASO spatial consistency plots show only axes of motion columns that are detected in both BOLD and VASO contrasts for each columnarity threshold (see animations here: https://doi.org/10.6084/m9.figshare.20393667.

on the pial surface (Kim et al. 2013), which is still disputed. We believe that our new local metrics of sensitivity and specificity provide an alternative way to evaluate the draining veins effect and to visualize pial vessels responsible for it.

General perspective on cortical columns

While the existence of direction selective neurons within area MT is a well-established feature in primates (Albright 1984) and cats (Hubel and Wiesel 1962, 1965) only preliminary fMRI evidence has been reported in humans (Zimmermann et al. 2011, De Martino et al. 2013). Our findings provide strong evidence for a functional columnar organization of axis-of-motion features also in human MT+. The obtained columnarity maps, however,

indicate that functional clusters are only partially in line with proposed ideal (anatomical) columnar models (Mountcastle 1956) that are assumed to penetrate vertically from the pial surface to the white matter boundary in a regular manner. The hypothesis of 3D columns was mostly investigated by multi-unit electrophysiological recordings in animals. Pioneering results from Hubel and Wiesel (1962, 1965), Albright et al. (1984), were put in perspective by reports showing that the preferred orientations were not necessarily represented in a columnar fashion in animal visual cortex (Bauer et al. 1983, Berman et al. 1987, Bauer et al. 1989). In particular, Bauer et al. (1983) reported that the preferred orientations jump by 90° along the vertical track of the electrode penetration in cat area 18. It's worth noting
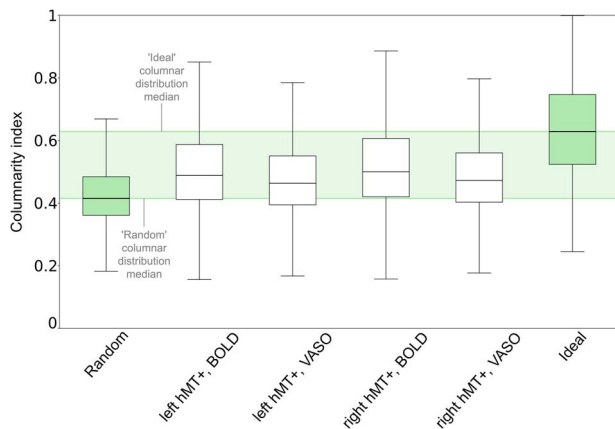
A) Left-hMT+
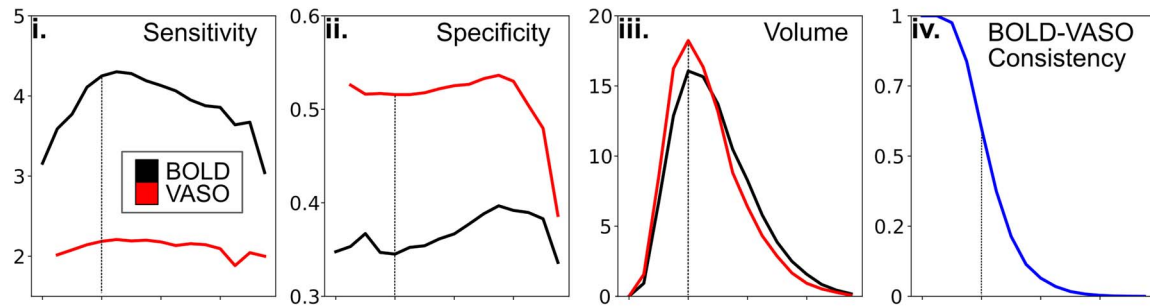
B) Right-hMT+
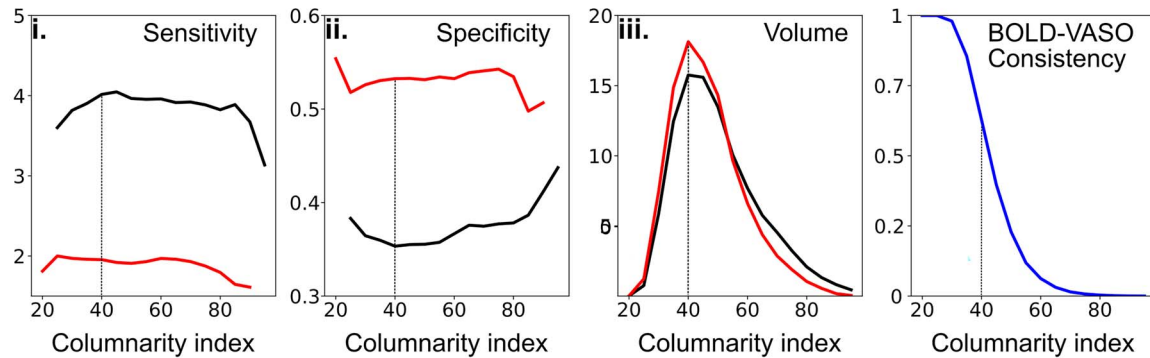
Fig. 9. Descriptive statistics for both BOLD and VASO columnarity maps in (A) left hMT+ and (B) right hMT+. Average of voxel-wise sensitivity (i) and specificity (ii) and percentage of columnar hMT+ volume (iii) is evaluated for both BOLD (black line) and VASO (red line) as a function of the columnarity index. (iv) Average of BOLD-VASO consistency quantified for each value of the columnarity index. A vertical dotted line is drawn for a columnarity index of 40, corresponding to the peak of columnar volume (iii).

Fig. 10. Comparing columnarity index distributions between empirical and benchmark datasets. Empirical BOLD and VASO group distributions of left-hMT+ and right-hMT+ are reported as white boxplots. 'Random' and 'ideal' columnarity index distributions are shown in green boxplots on the left and right side, respectively. Boxplots extend from the first quartile to the third quartile, with a line at the median. The whiskers extend from the box by 1.5x the iter-quartile range. Green shaded bands encompass the upper and lower distribution of the random and ideal benchmark sets. See Supplementary Fig. 4 for a detailed version with individual participant results.

that this technique comes with the cumbersome task of accurately tracing the penetrating electrodes together with the limited sampling space, affecting the robustness of those results (Horton and Adams 2005). Later findings (Tanaka et al. 2011) provided a new perspective on the conventional columnar view

of orientation representation of the visual cortex: simulations based on a 3D self-organized model predicted the occurrence of direction reversal in columns along the cortical depth dimension being proportional to the curvature of the cortex, and orientation columns having wedge-like shape when sampling gyri or sulci. The same study confirmed these theoretical predictions with multi-slice, high-resolution functional MRI in cat areas 17 and 18. These mechanisms were also discussed by (Zimmermann et al. 2011) to explain the variability of iso-oriented feature maps across cortical depths observed with high-resolution fMRI in humans. Recently, Nakamichi et al. (2018) proposed a new explanation for the variability across cortical depths based on functional optical coherence tomography in cats: their results show that the 3D structure of orientation columns were heavily distorted around pinwheel centers. Orientation singularities were rarely straight solid bars connecting pinwheel centers, instead they typically ran inside the cortex creating "singularity strings" with peculiar trajectories. Besides findings challenging a simplistic view of columnar organization (Rakic 2008), the functional relevance of cortical columns has also been debated (Horton and Adams 2005, Haueis 2021). Whether cortical columns "are a structure without a function" (Horton and Adams 2005) or not, the presence of functional clusters with groups of neurons that share similar tuning properties allows high-resolution human fMRI studies to reveal coding principles of the brain, which would otherwise only be possible at microscopic resolution.

Our columnar results are to our knowledge the first to provide a quantitative columnarity map to characterize the functional organization of axis-of-motion features in hMT+ exploiting the benefits of CBV-based fMRI at 7T. Our new algorithm for column

detection not only improved the quantifiability and comparability with other studies, but it also takes into account the curvature effect (Tanaka et al. 2011). However, we found that the spatial consistency between VASO and BOLD columnar results decreased as a function of the columnarity index. We believe that this variability is due to an interplay of two effects. On the one hand, the differences in terms of sensitivity but especially specificity between VASO and BOLD would mostly affect the columnar results when a conservative columnarity index threshold is applied. On the other hand, the aforementioned theory of variability of orientation selectivity across cortical depths could explain the trend of spatial consistency.

Future CBV-sensitive fMRI studies with higher spatial resolution (e.g. < 0.5 mm isotropic), improved sensitivity and increased sample size, would be able to investigate the functional organization of hMT+ in more detail that would be likely sufficient to resolve direction-of-motion columns instead of the larger axis-of-motion columns with higher statistical power. Such higher-resolution fMRI studies might also reveal direct evidence for pinwheels and their effect on columnarity.

Another critical aspect that has to be discussed while interpreting fMRI results on functional cortical columns is the link to the underlying vasculature, in particular to the influence of penetrating arteries and veins that run perpendicularly to the cortex. The review paper by Uludağ and Blinder (2018) dedicates a paragraph 'Vascular and columnar neuronal functional units' shedding light on this topic. Despite Blinder et al. (2013) convincingly showing no association between columnar responses and vasculature tree in the mouse barrel field cortex, a clear understanding of the same relationship in humans is still lacking. Conducting higher resolution fMRI studies would not resolve this conundrum by itself. Therefore, there is a need to understand the origin of the vascular control of the cerebral blood flow that sustains neurons along the whole vascular tree and how this interacts with mesoscopic cortical features such as columns and layers. A meaningful future direction would be to combine such higher-resolution fMRI studies together with even higher-resolution anatomical MRI data (e.g. < 0.4 iso mm, Lüsebrink et al. 2021, Bollmann et al. 2022, Gulban et al. 2022). For instance, conjoining the development of new VASO acquisition protocols (Koiso et al. 2022, Dresbach et al. 2023, Faes et al. 2023) with functional column responses (Yacoub et al. 2008, Hollander et al. 2021), and with the analysis of the in vivo intracortical angioarchitecture (Gulban et al. 2022, see Fig. 4) might offer a way to reveal if the detected columns are a reflection of the underlying macrovasculature in humans, or not.

To conclude, the improved quantifiability provided by our new method for column detection will make the comparison of our results with future studies straightforward. Furthermore, our approach and methodological developments are generalizable and applicable to other human brain areas where similar mesoscopic research questions are addressed.

Author contributions

According to the CRediT system (https://casrai.org/credit/) **Conceptualization:** A.P., R.H., O.F.G., R.G. **Methodology:** A.P., O.F.G., J.P., R.G. **Software:** A.P., O.F.G. **Validation:** A.P., R.H., O.F.G., R.G. **Formal Analysis:** A.P. **Investigation:** A.P., R.H., A.B.A. **Resources:** A.P., R.H., O.F.G., A.B.A., J.P., R.G. **Data curation:** A.P., A.B.A. **Writing – original draft:** A.P. **Writing – review & editing:** A.P., R.H., O.F.G., A.B.A., J.P., R.G. **Visualization:** A.P., R.H., O.F.G., R.G. **Supervision:** R.H., O.F.G., J.P., R.G. **Project administration:** R.H., J.P., R.G. **Funding acquisition:** R.G.

CRediT authors statement

Alessandra Pizzuti (Conceptualization, Data curation, Formal analysis, Investigation, Methodology, Resources, Software, Validation, Visualization, Writing–original draft, Writing–review & editing), Laurentius Huber (Conceptualization, Investigation, Methodology, Project administration, Resources, Supervision, Validation, Writing–review & editing), Faruk Gulban (Conceptualization, Investigation, Methodology, Resources, Software, Supervision, Validation, Visualization, Writing–review & editing), Amaia Benitez-Andonegui (Data curation, Investigation, Resources, Writing–review & editing), Judith Peters (Methodology, Project administration, Resources, Supervision, Writing–review & editing), Rainer Goebel (Conceptualization, Funding acquisition, Methodology, Project administration, Resources, Supervision, Validation, Visualization, Writing–review & editing).

Supplementary material

Supplementary material is available at *Cerebral Cortex* online.

Funding

Data and code availability statement

Analysis codes are available on github: https://github.com/27-apizzuti/AOM-VASO_project. A full overview of our processing pipeline is available here: https://github.com/27-apizzuti/AOM-VASO_project/tree/main/diagrams. Dataset is made available here: https://doi.org/10.5281/zenodo.7858649.

References

Albright TD. Direction and orientation selectivity of neurons in visual area MT of the macaque. *J Neurophysiol*. 1984:52:1106–1130. https://doi.org/10.1152/jn.1984.52.6.1106.

Albright TD, Desimone R, Gross CG. Columnar organization of directionally selective cells in visual area MT of the macaque. *J Neurophysiol*. 1984:51:16–31. https://doi.org/10.1152/jn.1984.51.1.16.

Ashburner J, Friston KJ. Unified segmentation. *NeuroImage*. 2005:26: 839–851. https://doi.org/10.1016/j.neuroimage.2005.02.018.

Avants BB, Tustison N, Song G. Advanced normalization tools (ANTS). *Insight J*. 2009:2:1–35.

Avants BB, Tustison NJ, Song G, Cook PA, Klein A, Gee JC. A reproducible evaluation of ANTs similarity metric performance in brain image registration. *NeuroImage*. 2011:54:2033–2044. https://doi.org/10.1016/j.neuroimage.2010.09.025.

Bauer R, Dow BM, Snyder AZ, Vautin R. Orientation shift between upper and lower layers in monkey visual cortex. *Exp Brain Res*. 1983:50:133–145. https://doi.org/10.1007/BF00238240.

Bauer R, Eckhorn R, Jordan W. Iso- and cross-oriented columns in cat striate cortex: a study with simultaneous single- and multi-unit recordings. *Neuroscience*. 1989:30:733–740. https://doi.org/10.1016/0306-4522(89)90165-6.

Beckett AJ, Dadakova T, Townsend J, Huber L, Park S, Feinberg DA. Comparison of BOLD and CBV using 3D EPI and 3D GRASE for cortical layer functional MRI at 7 T. *Magn Reson Med*. 2020:84:3128–3145. https://doi.org/10.1002/mrm.28347.

Berman NE, Wilkes ME, Payne BR. Organization of orientation and direction selectivity in areas 17 and 18 of cat cerebral cortex. *J Neurophysiol*. 1987:58:676–699. https://doi.org/10.1152/jn.1987.58.4.676.

Blazejewska AI, Fischl B, Wald LL, Polimeni JR. Intracortical smoothing of small-voxel fMRI data can provide increased detection power without spatial resolution losses compared to conventional large-voxel fMRI data. *NeuroImage*. 2019:189:601–614. https://doi.org/10.1016/j.neuroimage.2019.01.054.

Blinder P, Tsai PS, Kaufhold JP, Knutsen PM, Suhl H, Kleinfeld D. The cortical angiome: an interconnected vascular network with non-columnar patterns of blood flow. *Nat Neurosci*. 2013:16:889–897. https://doi.org/10.1038/nn.3426.

Bok ST. *Histonomy of the cerebral cortex*. Elsevier Publishing Company, 1959. https://books.google.nl/books?id=sdIEAQAAIAAJ.

Bollmann S, Mattern H, Bernier M, Robinson SD, Park D, Speck O, Polimeni JR. Imaging of the pial arterial vasculature of the human brain in vivo using highresolution 7T time-of-flight angiography. *eLife* 2022:11:1–35. https://doi.org/10.7554/eLife.71186.

Born RT, Bradley DC. Structure and function of visual area MT. *Annu Rev Neurosci*. 2005:28:157–189. https://doi.org/10.1146/annurev.neuro.26.041002.131052.

Breman H, Mulders J, Fritz L, Peters J, Pyles J, Eck J, Bastiani M, Roebroeck A, Ashburner J, Goebel R. An image registration-based method for epi distortion correction based on opposite phase encoding (COPE), in: lecture notes in computer science (including subseries lecture notes in artificial intelligence and lecture notes in bioinformatics). *Springer. p*. 2020:122–130. https://doi.org/10.1007/978-3-030-50120-4_12.

Buxhoeveden DP, Casanova MF. The minicolumn hypothesis in neuroscience. *Brain*. 2002:125:935–951. https://doi.org/10.1093/brain/awf110.

Cho S, Roy A, Liu CJ, Idiyatullin D, Zhu W, Zhang Y, Zhu XH, O'Herron P, Leikvoll A, Chen W, et al. Cortical layer-specific differences in stimulus selectivity revealed with high-field fMRI and single-vessel resolution optical imaging of the primary visual cortex. *NeuroImage*. 2022:251:1–13. https://doi.org/10.1016/j.neuroimage.2022.118978.

Cox RW. AFNI: software for analysis and visualization of functional magnetic resonance neuroimages. *Computers and Biomedical Research* 1996:29(3):162–173. https://doi.org/10.1006/cbmr.1996.0014.

Cox RW, Hyde JS. Software tools for analysis and visualization of FMRI data NMR in biomedicine, in press. *NMR Biomed*. 1997:10:171–178. https://afni.nimh.nih.gov/pub/dist/doc/papers/afni_paper2.pdf.

De Martino F, Zimmermann J, Muckli L, Ugurbil K, Yacoub E, Goebel R. Cortical depth dependent functional responses in humans at 7T: improved specificity with 3D GRASE. *PLoS One*. 2013:8:1–14. https://doi.org/10.1371/journal.pone.0060514.

De Martino F, Moerel M, Ugurbil K, Goebel R, Yacoub E, Formisano E. Frequency preference and attention effects across cortical depths in the human primary auditory cortex. *Proc Natl Acad Sci U S A*. 2015:112:16036–16041. https://doi.org/10.1073/pnas.1507552112.

De Martino F, Yacoub E, Kemper V, Moerel M, Uludag K, De Weerd P, Ugurbil K, Goebel R, Formisano E. The impact of ultra-high field MRI on cognitive and computational neuroimaging. *NeuroImage*. 2018:168:366–382. https://doi.org/10.1016/j.neuroimage.2017.03.060.

Diogo ACM, Soares JG, Koulakov A, Albright TD, Gattass R. Electrophysiological imaging of functional architecture in the cortical middle temporal visual area of Cebus apella monkey. *J Neurosci*. 2003:23:3881–3898. https://doi.org/10.1523/jneurosci.23-09-03881.2003.

Dresbach S, Huber R, Gulban OF, Goebel R. Fast layer-fMRI VASO with short stimuli and event-related designs at 7T. *bioRxiv*. 2023:1–32. https://www.biorxiv.org/content/ https://doi.org/10.1101/2023.03.15.532735v1.full.pdf, https://doi.org/10.1101/2023.03.15.532735.

Dumoulin SO, Fracasso A, van der Zwaag W, Siero JC, Petridou N. Ultra-high field MRI: advancing systems neuroscience towards mesoscopic human brain function. *NeuroImage* 2018:168:345–357. https://doi.org/10.1016/j.neuroimage.2017.01.028.

Duvernoy HM, Delon S, Vannson JL. Cortical blood vessels of the human brain. *Brain Res Bull*. 1981:7:519–579. https://doi.org/10.1016/0361-9230(81)90007-1.

Emmerling TC. Maastricht University, The Netherlands. 2016. https://doi.org/10.26481/dis.20160622te.

Faes LK, De Martino F, Huber L. Cerebral blood volume sensitive layer-fMRI in the human auditory cortex at 7T: challenges and capabilities. *PLoS One*. 2023:18:1–22. https://doi.org/10.1371/journal.pone.0280855.

Feinberg DA, Kiefer B, Johnson G. GRASE improves spatial resolution in single shot imaging. *Magn Reson Med*. 1995:33:529–533. https://doi.org/10.1002/mrm.1910330411.

Friston KJ, Ashburner JT, Kiebel SJ, Nichols TE, Penny WD. Statistical parametric mapping: the analysis of functional brain images. *Elsevier* 2007:8:1–647. http://books.elsevier.com/neuro/?isbn=9780123725608&srccode=89660.

Glover GH, Li TQ, Ress D. Image-based method for retrospective correction of physiological motion effects in fMRI: RETROICOR. *Magn Reson Med*. 2000:44:162–167. https://doi.org/10.1002/1522-2594(200007)44:1(162::aid-mrm23)3.3.co;2-5.

Goebel R, Khorram-Sefat D, Muckli L, Hacker H, Singer W. The constructive nature of vision: direct evidence from functional magnetic resonance imaging studies of apparent motion and motion imagery. *Eur J Neurosci*. 1998:10:1563–1573. https://doi.org/10.1046/j.1460-9568.1998.00181.x.

Goebel R, Esposito F, Formisano E. Analysis of functional image analysis contest (FIAC) data with BrainVoyager QX: from single-subject to cortically aligned group general linear model analysis and self-organizing group independent component analysis. *Hum Brain Mapp*. 2006:27:392–401. https://doi.org/10.1002/hbm.20249.

Goebel R, Muckli L, Kim DS. Visual system. *The Human Nervous System*. 2012:1301–1327. https://doi.org/10.1016/B978-0-12-374236-0.10037-9.

Guidi M, Huber L, Lampe L, Merola A, Ihle K, Möller HE. Cortical laminar resting-state signal fluctuations scale with the hypercapnic blood oxygenation level-dependent response. *Hum Brain Mapp*. 2020:41:2014–2027. https://doi.org/10.1002/hbm.24926.

Gulban OF. The relation between color spaces and compositional data analysis demonstrated with magnetic resonance image processing applications. *Austrian Journal of Statistics*. 2018:47:34–46. https://doi.org/10.17713/ajs.v47i5.743.

Gulban OF, Schneider M, Marquardt I, Haast RA, De Martino F. A scalable method to improve gray matter segmentation at ultra high field MRI. *PLoS One*. 2018:13:1–31. https://doi.org/10.1371/journal.pone.0198335.

Gulban OF, Bollmann S, Huber R, Wagstyl K, Goebel R, Poser BA, Kay K, Ivanov D. Mesoscopic in vivo human T2∗ dataset acquired using quantitative MRI at 7 tesla. *NeuroImage*. 2022:264:119733. https://doi.org/10.1016/j.neuroimage.2022.119733.

Haenelt D, Trampel R, Nasr S, Polimeni JR, Tootell RB, Sereno MI, Pine KJ, Edwards LJ, Helbling S, Weiskopf N. High-resolution quantitative and functional MRI indicate lower myelination of thin and thick stripes in human secondary visual cortex. *elife*. 2023:12:1–33. https://doi.org/10.7554/elife.78756.

Haueis P. The death of the cortical column? Patchwork structure and conceptual retirement in neuroscientific practice. *Stud Hist Phil Sci*. 2021:85:101–113. https://doi.org/10.1016/j.shpsa.2020.09.010.

Hollander G DE, van der Zwaag W, Qian C, Zhang P, Knapen T. Ultra-high field fMRI reveals origins of feedforward and feedback activity within laminae of human ocular dominance columns. *NeuroImage* 2021:228:117683. https://doi.org/10.1016/j.neuroimage.2020.117683.

Horton JG, Adams DL. The cortical column: a structure without a function. *Philos Trans R Soc B: Biol Sci*. 2005:360:837–862. https://doi.org/10.1098/rstb.2005.1623.

Hua J, Jones CK, Qin Q, Van Zijl PC. Implementation of vascular-space-occupancy MRI at 7T. *Magn Reson Med*. 2013:69:1003–1013. https://doi.org/10.1002/mrm.24334.

Hubel DH, Wiesel TN. Receptive fields, binocular interaction and functional architecture in the cat's visual cortex. *J Physiol*. 1962:160:106–154. https://onlinelibrary.wiley.com/doi/10.1113/jphysiol.1962.sp006837.

Hubel DH, Wiesel TN. Receptive fields and functional architecture in two nonstriate visual areas (18 and 19) of the cat. *J Neurophysiol*. 1965:28:229–289. http://www.ncbi.nlm.nih.gov/pubmed/14283058, http://www.physiology.org/doi/10.1152/jn.1965.28.2.229.

Huber L. Mapping human brain activity by functional magnetic resonance imaging of blood volume. Ph.D. thesis. Volume D, Max Plank Institute, Leipzig, Germany, 2015, 1–277, http://nbn-resolving.de/urn:nbn:de:bsz:15-qucosa-165252.

Huber L, Ivanov D, Krieger SN, Streicher MN, Mildner T, Poser BA, Möller HE, Turner R. Slab-selective, BOLD-corrected VASO at 7 tesla provides measures of cerebral blood volume reactivity with high signal-to-noise ratio. *Magn Reson Med*. 2014:72:137–148. https://doi.org/10.1002/mrm.24916.

Huber L, Goense J, Kennerley AJ, Trampel R, Guidi M, Reimer E, Ivanov D, Neef N, Gauthier CJ, Turner R, et al. Cortical lamina-dependent blood volume changes in human brain at 7T. *NeuroImage*. 2015:107:23–33. https://doi.org/10.1016/j.neuroimage.2014.11.046.

Huber L, Handwerker DA, Jangraw DC, Chen G, Hall A, Stüber C, Gonzalez-Castillo J, Ivanov D, Marrett S, Guidi M, et al. High-resolution CBV-fMRI allows mapping of laminar activity and connectivity of cortical input and output in human M1. *Neuron*. 2017:96:1253–1263. https://doi.org/10.1016/j.neuron.2017.11.005.

Huber L, Ivanov D, Handwerker DA, Marrett S, Guidi M, Uludağ K, Bandettini PA, Poser BA. Techniques for blood volume fMRI with VASO: from low-resolution mapping towards sub-millimeter layer-dependent applications. *NeuroImage*. 2018:164:131–143. https://doi.org/10.1016/j.neuroimage.2016.11.039.

Huber L, Uludağ K, Möller HE. Non-BOLD contrast for laminar fMRI in humans: CBF, CBV, and CMRO2. *NeuroImage*. 2019:197:742–760. https://doi.org/10.1016/j.neuroimage.2017.07.041.

Huber L, Finn ES, Chai Y, Goebel R, Stirnberg R, Stöcker T, Marrett S, Uludag K, Kim SG, Han SH, Bandettini PA, Poser BA. Layerdependent functional connectivity methods. *Progress in Neurobiology*. 2020:(January):101835. https://doi.org/10.1016/j.pneurobio.2020.101835.

Huber LR, Poser BA, Bandettini PA, Arora K, Wagstyl K, Cho S, Goense J, Nothnagel N, Morgan AT, van den Hurk J, Müller AK, Reynolds RC, Glen DR, Goebel R, Gulban OF. LayNii: a software suite for layer-fMRI. *NeuroImage* 2021:237:1–19, 118091. https://doi.org/10.1016/j.neuroimage.2021.118091.

Huk AC, Dougherty RF, Heeger DJ. Retinotopy and functional subdivision of human areas MT and MST. *J Neurosci*. 2002:22:7195–7205. https://www.jneurosci.org/lookup/doi/10.1523/JNEUROSCI.22-16-07195.2002.

Kay K, Jamison KW, Vizioli L, Zhang R, Margalit E, Ugurbil K. A critical assessment of data quality and venous effects in sub-millimeter fMRI. *NeuroImage*. 2019:189:847–869. https://doi.org/10.1016/j.neuroimage.2019.02.006.

Kemper VG, De Martino F, Vu AT, Poser BA, Feinberg DA, Goebel R, Yacoub E. Sub-millimeter T2 weighted fMRI at 7 T: comparison of 3D-GRASE and 2D SE-EPI. *Front Neurosci*. 2015:9:1–14. https://doi.org/10.3389/fnins.2015.00163.

Kim SG, Harel N, Jin T, Kim T, Lee P, Zhao F. Cerebral blood volume MRI with intravascular superparamagnetic iron oxide nanoparticles. *NMR Biomed*. 2013:26:949–962. https://doi.org/10.1002/nbm.2885.

Koiso K, Müller AK, Akamatsu K, Dresbach S, Wiggins CJ, Gulban OF, Goebel R, Miyawaki Y, Poser BA, Huber L. Acquisition and processing methods of whole-brain layer-fMRI VASO and BOLD: the Kenshu dataset. *Neuroscience* 2022. https://doi.org/10.1101/2022.08.19.504502.

Kolster H, Peeters R, Orban GA. The retinotopic organization of the human middle temporal area MT/V5 and its cortical neighbors. *J Neurosci*. 2010:30:9801–9820. https://doi.org/10.1523/JNEUROSCI.2069-10.2010.

Koopmans PJ, Yacoub E. Strategies and prospects for cortical depth dependent T2 and T2∗ weighted BOLD fMRI studies. *NeuroImage*. 2019:197:668–676. https://doi.org/10.1016/j.neuroimage.2019.03.024.

Lauwers F, Cassot F, Lauwers-Cances V, Puwanarajah P, Duvernoy H. Morphometry of the human cerebral cortex microcirculation: general characteristics and space-related profiles. *NeuroImage*. 2008:39:936–948. https://doi.org/10.1016/j.neuroimage.2007.09.024.

Lu H, Golay X, Pekar JJ, Van Zijl PC. Functional magnetic resonance imaging based on changes in vascular space occupancy. *Magn Reson Med*. 2003:50:263–274. https://doi.org/10.1002/mrm.10519. https://pubmed.ncbi.nlm.nih.gov/12876702/.

Lüsebrink F, Mattern H, Yakupov R, Acosta-Cabronero J, Ashtarayeh M, Oeltze-Jafra S, Speck O. Comprehensive ultrahigh resolution whole brain in vivo MRI dataset as a human phantom. *Scientific Data*. 2021:8:1–13. https://doi.org/10.1038/s41597-021-00923-w.

Madge V, 2020. *Evaluating Voxelmorph: a learning-based 3D non-linear registration algorithm, against the non-linear symmetric normalization technique from ANTs*. Ph.D. thesis. McGill University, Montreal, Quebec, Canada. https://escholarship.mcgill.ca/concern/theses/zp38wj23v.

Malonek D, Tootell RB, Grinvald A. Optical imaging reveals the functional architecture of neurons processing shape and motion in owl monkey area MT. *Proc R Soc B Biol Sci*. 1994:258:109–119. https://doi.org/10.1098/rspb.1994.0150.

Marques JP, Kober T, Krueger G, Zwaag W van der, Van de Moortele PF, Gruetter R. MP2RAGE, a self bias-field corrected sequence for improved segmentation and T1-mapping at high field. *NeuroImage*. 2010:49:1271–1281. https://doi.org/10.1016/j.neuroimage.2009.10.002.

Maunsell JH, Van Essen DC. Functional properties of neurons in middle temporal visual area of the macaque monkey. I. Selectivity for stimulus direction, speed, and orientation. *J Neurophysiol*. 1983:49:1127–1147. https://doi.org/10.1152/jn.1983.49.5.1127.

Moeller S, Yacoub E, Olman CA, Auerbach E, Strupp J, Harel N, Uğurbil K. Multiband multislice GE-EPI at 7 tesla, with 16-fold acceleration using partial parallel imaging with application to high spatial and temporal whole-brain FMRI. *Magn Reson Med*. 2010:63:1144–1153. https://doi.org/10.1002/mrm.22361.

Mountcastle VB. Modality and topographic properties neurons of cat ' S somatic sensory. *Journal of Neurophisiology* 1956:20:408–434. https://doi.org/10.1152/jn.1957.20.4.408.

Mountcastle VB. The columnar organization of the neocortex. *Brain*. 1997:120:701–722. https://doi.org/10.1093/brain/120.4.701.

Muckli L, Kriegeskorte N, Lanfermann H, Zanella FE, Singer W, Goebel R. Apparent motion: event-related functional magnetic resonance imaging of perceptual switches and states. *J Neurosci*. 2002:22:1–5. https://doi.org/10.1523/jneurosci.22-09-j0003.2002.

Nakamichi Y, Kalatsky VA, Watanabe H, Sato T, Rajagopalan UM, Tanifuji M. 3D topology of orientation columns in visual cortex revealed by functional optical coherence tomography. *J Neurophysiol*. 2018:119:1562–1575. https://doi.org/10.1152/jn.00921.2017.

Oliveira IA, Cai Y, Hofstetter S, Siero JC, van der Zwaag W, Dumoulin SO. Comparing BOLD and VASO-CBV population receptive field estimates in human visual cortex. *NeuroImage*. 2022:248:1–11. https://doi.org/10.1016/j.neuroimage.2021.118868.

Oshio K, Feinberg DA. Single-shot GRASE imaging without fast gradients. *Magn Reson Med*. 1992:26:355–360. https://doi.org/10.1002/mrm.1910260214.

Petro LS, Muckli L. The laminar integration of sensory inputs with feedback signals in human cortex. *Brain Cogn*. 2017:112:54–57. https://doi.org/10.1016/j.bandc.2016.06.007.

Poser BA, Koopmans PJ, Witzel T, Wald LL, Barth M. Three dimensional echo-planar imaging at 7 tesla. *NeuroImage*. 2010:51:261–266. https://doi.org/10.1016/j.neuroimage.2010.01.108.

Rakic P. Confusing cortical columns. *Proc Natl Acad Sci U S A*. 2008:105:12099–12100. https://doi.org/10.1073/pnas.0807271105.

Rees G, Friston K, Koch C. A direct quantitative relationship between the functional properties of human and macaque V5. *Nat Neurosci*. 2000:3:716–723. https://doi.org/10.1038/76673. http://neurosci.nature.com.

Schneider M, Kemper VG, Emmerling TC, De Martino F, Goebel R. Columnar clusters in the human motion complex reflect consciously perceived motion axis. *Proc Natl Acad Sci U S A*. 2019:116:5096–5101. https://doi.org/10.1073/pnas.1814504116.

Shmuel A, Yacoub E, Chaimow D, Logothetis NK, Ugurbil K. Spatio-temporal point-spread function of fMRI signal in human gray matter at 7 tesla. *NeuroImage*. 2007:35:539–552. https://doi.org/10.1016/j.neuroimage.2006.12.030. https://www.ncbi.nlm.nih.gov/pmc/articles/PMC3624763/pdf/nihms412728.pdf, https://linkinghub.elsevier.com/retrieve/pii/S1053811906012444.

Smith SM, Jenkinson M, Woolrich MW, Beckmann CF, Behrens TE, Johansen-Berg H, Bannister PR, De Luca M, Drobnjak I, Flitney DE, Niazy RK, Saunders J, Vickers J, Zhang Y, De Stefano N, Brady JM, Matthews PM. Advances in functional and structural MR image analysis and implementation as FSL, in: NeuroImage. 2004. www.sciencedirect.com, https://doi.org/doi:10.1016/j.neuroimage.2004.07.051.

Sullivan C, Kaszynski A. PyVista: 3D plotting and mesh analysis through a streamlined interface for the visualization toolkit (VTK). *J Open Source Software*. 2019:4:1450. https://doi.org/10.21105/joss.01450.

Swindale NV. Orientation tuning curves: empirical description and estimation of parameters. *Biol Cybern*. 1998:78:45–56. https://doi.org/10.1007/s004220050411.

Talagala SL, Sarlls JE, Liu S, Inati SJ. Improvement of temporal signal-to-noise ratio of GRAPPA accelerated echo planar imaging using a FLASH based calibration scan. *Magn Reson Med*. 2016:75:2362–2371. https://doi.org/10.1002/mrm.25846.

Tanaka S, Moon CH, Fukuda M, Kim SG. Three-dimensional visual feature representation in the primary visual cortex. *Neural Netw*. 2011:24:1022–1035. https://doi.org/10.1016/j.neunet.2011.05.005.

Tootell RB, Reppas JB, Kwong KK, Malach R, Born RT, Brady TJ, Rosen BR, Belliveau JW. Functional analysis of human MT and related visual cortical areas using magnetic resonance imaging. *J Neurosci*. 1995:15:3215–3230. https://doi.org/10.1523/jneurosci.15-04-03215.1995.

Triantafyllou C, Hoge RD, Krueger G, Wiggins CJ, Potthast A, Wiggins GC, Wald LL. Comparison of physiological noise at 1.5 T, 3 T and 7 T and optimization of fMRI acquisition parameters. *NeuroImage*. 2005:26:243–250. https://doi.org/10.1016/j.neuroimage.2005.01.007.

Ugurbil K. What is feasible with imaging human brain function and connectivity using functional magnetic resonance imaging. *Philosophical Transactions of the Royal Society B: Biological Sciences* 2016:371. https://doi.org/10.1098/rstb.2015.0361.

Uğurbil K. Ultrahigh field and ultrahigh resolution fMRI. *Current Opinion in Biomedical Engineering*. 2021:18. https://doi.org/10.1016/j.cobme.2021.100288.

Uğurbil K, Adriany G, Andersen P, Chen W, Garwood M, Gruetter R, Henry PG, Kim SG, Lieu H, Tkac I, et al. Ultrahigh field magnetic resonance imaging and spectroscopy. *Magn Reson Imaging*. 2003:21:1263–1281. https://doi.org/10.1016/j.mri.2003.08.027.

Uludağ K, Blinder P. *Linking brain vascular physiology to hemodynamic response in ultra-high field MRI*. 2018:168:279–295. https://doi.org/10.1016/j.neuroimage.2017.02.063.

Uludağ K, Müller-Bierl B, Uğurbil K. An integrative model for neuronal activity-induced signal changes for gradient and spin echo functional imaging. *NeuroImage*. 2009:48:150–165. https://doi.org/10.1016/J.NEUROIMAGE.2009.05.051.

Viessmann O, Polimeni JR, 2021. High-resolution fMRI at 7 tesla: challenges, promises and recent developments for individual-focused fMRI studies. *Curr Opin Behav Sci*40, 96–104. https://doi.org/10.1016/j.cobeha.2021.01.011.

Virtanen P, Gommers R, Oliphant TE, Haberland M, Reddy T, Cournapeau D, Burovski E, Peterson P, Weckesser W, Bright J, et al. SciPy 1.0: fundamental algorithms for scientific computing in python. *Nat Methods*. 2020:17:261–272. https://doi.org/10.1038/s41592-019-0686-2. http://www.nature.com/articles/s41592-019-0686-2.

Waehnert MD, Dinse J, Weiss M, Streicher MN, Waehnert P, Geyer S, Turner R, Bazin PL. Anatomically motivated modeling of cortical laminae. *NeuroImage*. 2014:93:210–220. https://doi.org/10.1016/j.neuroimage.2013.03.078.

Watson JD, Shipp S, Zeki S, Watson JD, Myers R, Frackowiak RS, Hajnal JV, Woods RP, Mazziotta JC. Area v5 of the human brain: evidence from a combined study using positron emission tomography and magnetic resonance imaging. *Cereb Cortex*. 1993:3:79–94. https://doi.org/10.1093/cercor/3.2.79.

Weber B, Weber B, Keller AL, Reichold J, Logothetis NK. The microvascular system of the striate and extrastriate visual cortex of the macaque. *Cereb Cortex*. 2008:18:2318–2330. https://doi.org/10.1093/cercor/bhm259.

Yacoub E, Harel N, Uğurbil K. High-field fMRI unveils orientation columns in humans. *Proc Natl Acad Sci U S A*. 2008:105:10607–10612. https://doi.org/10.1073/pnas.0804110105.

Yushkevich PA, Piven J, Hazlett HC, Smith RG, Ho S, Gee JC, Gerig G. User-guided 3D active contour segmentation of anatomical structures: significantly improved efficiency and reliability. *NeuroImage*. 2006:31:1116–1128. https://doi.org/10.1016/j.neuroimage.2006.01.015.

Zeki SM. Functional organization of a visual area in the posterior bank of the superior temporal sulcus of the rhesus monkey. *J Physiol*. 1974:236:549–573. https://onlinelibrary.wiley.com/doi/10.1113/jphysiol.1974.sp010452.

Zimmermann J, Goebel R, de Martino F, van de Moortele PF, Feinberg D, Adriany G, Chaimow D, Shmuel A, Uğurbil K, Yacoub E. Mapping the organization of axis of motion selective features in human area mt using high-field fmri. *PLoS One*. 2011:6:1–10. https://doi.org/10.1371/journal.pone.0028716.